Drone Based Evaluation of Spatial Variability in Satellite Surface Reflectance Products

드론을 활용한 위성 지표반사도 산출물 공간 패턴 분석

August 2021

**Graduate School of
Seoul National University**

Department of Landscape Architecture and Rural Systems Engineering, Landscape Architecture Major

Choi, Wonseok

Drone Based Evaluation of Spatial Variability in Satellite Surface Reflectance Products

Under the Direction of Adviser, Prof. Ryu, Youngryel

Submitting a master's thesis of Landscape Architecture

August, 2021

Graduate School of
Seoul National University
Department of Landscape Architecture and Rural Systems Engineering, Landscape Architecture Major

Choi, Wonseok

Confirming the master's thesis written by
Choi, Wonseok
July, 2021

Chair	Dong Kun Lee
Vice Chair	Youngryel Ryu
Examiner	

Abstract

High-resolution satellites are assigned to monitor land surface in detail. The reliable surface reflectance (SR) is the fundamental in terrestrial ecosystem modeling so the temporal and spatial validation is essential. Usually based on multiple ground control points (GCPs), field spectroscopy guarantees the temporal continuity. Due to limited sampling, however, it hardly illustrates the spatial pattern. As a map, the pixelwise spatial variability of SR products is not well-documented. In this study, we introduced drone-based hyperspectral image (HSI) as a reference and compared the map with Sentinel 2 and Landsat 8 SR products on a heterogeneous rice paddy landscape. First, HSI was validated by field spectroscopy and swath overlapping, which assured qualitative radiometric accuracy within the viewing geometry. Second, HSI was matched to the satellite SRs. It involves spectral and spatial aggregation, co-registration and nadir bidirectional reflectance distribution function (BRDF)-adjusted reflectance (NBAR) conversion. Then, we 1) quantified the spatial variability of the satellite SRs and the vegetation indices (VIs) including NDVI and NIRv by APU matrix, 2) qualified them pixelwise by theoretical error budget and 3) examined the improvement by BRDF normalization.

Sentinel 2 SR exhibits overall good agreement with drone HSI while the two NIRs are biased up to 10%. Despite the bias in NIR, the NDVI shows a good match on vegetated areas and the NIRv only displays the discrepancy on built-in areas. Landsat 8 SR was biased over the VIS bands (-9 ~ -7.6%). BRDF normalization just contributed to a minor improvement. Our results demonstrate the potential of drone HSI to replace in-situ observation and evaluate SR or atmospheric correction algorithms over the flat terrain. Future researches should replicate the results over the complex terrain and canopy structure (i.e. forest).

Keyword: Drone, Validation, Sentinel 2, Landsat 8, Surface reflectance, BRDF

Student Number: 2019-28352

Table of Contents

List of Figures

List of Tables

Chapter 1. Introduction

1.1 Background

Satellite remote sensing is based on linking surface reflectance to surface information, such as LAI, chlorophyll etc. The reliable SR is essential from a simple spectral ratio to radiative transfer modeling. However, the spectral relationship is commonly non-linear. Only spectral relationship could make a misleading, depending on the observed scale. The mismatch in spatial scales is a challenge to relate field to satellites observations (Kamal et al., 2016; Wang et al., 2014).

High resolution satellites enable spatial-explicit modeling of ecological properties. Directly relating plot level information to the SR on the according pixel, many studies monitored fine-scale dynamic, such as crown-scale phenology (Wu et al., 2021; Dixon et al., 2021; Vrieling et al., 2018), LAI (Kimm et al., 2020; Kamal et al., 2016), etc. Recent advances in CubeSat spurs the finer spatio-temporal monitoring of land surface (Houborg & McCabe, 2018; Houborg & McCabe, 2016b). Beyond the visual inspection, quantitative spatial analysis becomes more and more important.

These spatial analyses are only guaranteed by the consistency between the field plot and the satellite pixel. However, the pixel is distorted during the map processing (Duveiller & Defourny, 2010; Tan et al., 2006; Teillet, 1997). As a map, satellite SR product involves resampling and reprojection. The former is usually carried out for the better radiometric quality and the latter for the utility. Both accompany spatial interpolation. For example, Landsat Multi Spectral Sensor and AVHRR over-samples their observations, which enhance the radiometric quality (Duveiller & Defourny, 2010). In spite of the congruence between the native GSD and the pixel size, Landsat 8 and Sentinel 2 are resampled to universal transverse Mercator (UTM) grid by cubic and spline convolution, respectively (Zanter, 2019; Drusch et al., 2012). Wherein the map processing focuses on the misregistration, it still remains uncertain whether the SR on the spatial pixel well-represent the corresponding surface (Drusch et al., 2012; Tan et al., 2006).

For the application to quantitative spatial analysis, the evaluation should consider the spatial unit of the SR product. Traditionally, satellite SR products were evaluated in two aspect. The one is evaluating the sensor and the other one is evaluating the map. In the former aspect, SR is considered as a medium linking surface to satellite so it is rather referred to validate the sensor: the calibration, the degradation, the impact of spectral response function etc. (Lanconelli et al., 2020; Bruegge et al., 2019; Kharbouche et al., 2017; Ke et al., 2015; Teillet et al., 2007). It requires to reduce the possible noises. Homogeneous sites are preferred with temporal observations in several GCPs. Focusing on the sensor itself, it has no interest in the

spatial unit. In the latter aspect, SR is regarded as a map which the satellite produces. The map is validated at the pixel level: the spatial pattern, the impact of the gridding etc. (Planet, 2021; Claverie et al., 2018; Claverie et al., 2015; Peng et al., 2015). It requires pixel to pixel comparison. The finer map is aggregated to the coarser SR map and then compared to each other (Claverie et al., 2015). In the case of high-resolution SR map, however, the aggregation accompanies the enhancement in radiometric quality (Planet, 2021; Claverie et al., 2018; Claverie et al., 2015). The evaluation unit does not represent the original quality and loses the original spatial benefit.

The evaluation requests subpixel information. One classical method is comparing field spectroscopy to the pixels on the satellite SR product (Kong et al., 2021). Subpixel information was constructed by averaging several field measurements within the corresponding pixels. Based on a few GCPs, however, field spectroscopy tends to be biased (Asner et al., 2017; Rocha et al., 2019; Rocha et al., 2018). The scarcity of the sampling could induce the misregistration between GCPs and the corresponding pixels, the geographic error of which sometimes exceeds a unit pixel (Yan et al., 2016; Planet, 2021). Even worse, the spatial autocorrelation blurs the error. In spite of a significant misregistration, it could make a plausible result (Rocha et al., 2019; Rocha et al., 2018).

Recent advances in low altitude imaging spectroscopy, such as drone and airborne, enable collecting a vast amount of SR. As for figuring out the spatial pattern, it shows more reliable results than in-situ observations (Asner et al., 2017). Many studies proved its ability to replace field spectroscopy (Fawcett et al., 2020; Barreto et al., 2019; Cao et al., 2019; Hakala et al., 2018). However, most studies are limited to assess vegetation indices (Fawcett et al., 2020; Di Gennaro et al., 2019). Little considerations were given to the SR product (Seidel et al., 2018). Seidel et al. (2018) referred to airborne hyperspectral and evaluated Landsat 8. They successfully assessed Landsat 8 by means of BRDF effect in a diverse landcover types and prove the potential of HSI to emulate satellite SR products. Referring to the only two lines (along-track and cross-track), however, the spatial pattern was not well-documented. As they pointed out, the pixel size of the airborne map was 16 m so the slight scale mismatch makes it unclear to assess the impact of spatial convolution or geographical error.

In this study, we introduced drone HSI as a reference and compared the map with Sentinel 2 and Landsat 8 SR products on a heterogeneous rice paddy landscape. First, we assessed drone HSI in terms of the radiometric accuracy and BRDF effect. Second, HSI was matched to satellite SRs in terms of spatial resolution, spectral response and coordinates. To make viewing geometry consistent, both HSI and satellite SRs were converted to nadir bidirectional reflectance distribution function

(BRDF)-adjusted reflectance (NBAR) by global mean BRDF parameters. At the NBAR level, we 1) quantified the spatial variability of the satellite SRs and the vegetation indices (VIs) including NDVI and NIRv by APU matrix, 2) qualified them pixelwise by theoretical error budget and 3) examined the improvement by BRDF normalization.

Chapter 2. Method

2.1 Study Site
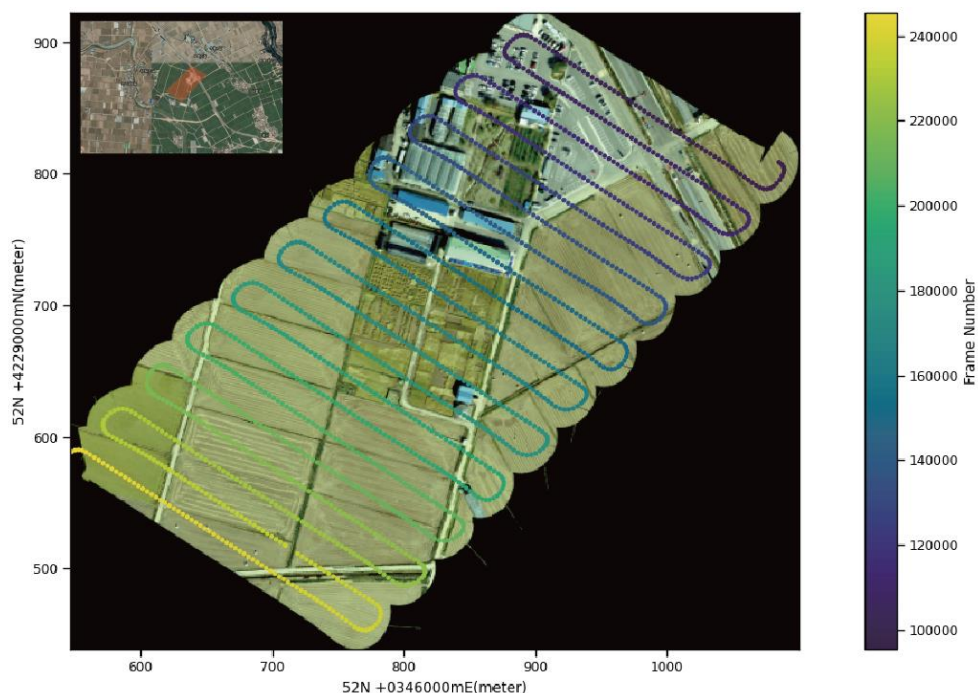
Figure 1 The top left map is a key map and the red area is our study site. The center image was acquired by drone. Dots on the image indicate the drone flight line. The color represents the relative time described as the frame number.

Our site is a rice paddy landscape located in Cheorwon, Gangwon province, South Korea (38.2018 N, 127.2507 E). Field campaign was carried out during the harvest season. It shows highly heterogenous landscape, including rice paddies, rice straws, colored rooftop, roads and parking lots. Though harvested, there remained other plants, beans, on the boundaries among paddies. Belonged to Korea Flux Network Site, one of rice paddy was sparsely sampled.

2.2   Drone campaign

   Drone campaign was carried out in Oct 7th, equipping a hyperspectral imager to the hexacopter, DJI M600 Pro. We use Headwall Nano hyperspectral imager. It is a push-broom sensor, consisting of a 640 spatial pixel array and 273 spectral bands in a 21.1 deg of angular field of view. Namely, a frame consists of 640 spatial pixels and a pixel contains 273 bands. It could cover 400 ~ 1000 nm with 6 nm full width half maximum (FWHM) and around 2.2 nm sampling interval (Barreto et al., 2019; Table 1). Before flight, we collected 500 dark and white frames, the former with lens capped and the latter on the 99 % Spectralon, which is near Lambertian. Dark noise was quantified by averaging dark frames. White frames were also averaged and later used for sensor calibration (sensor calibration part). Integration time was set to 4 ms, where all the bands were not saturated on the 99 % Spectralon. Flight plan was designed by UgCS software. It includes 21 flight lines with 7 cm native GSD and 50 % horizontal overlapping. On autopilot mode, the drone flew at a speed of 8 m/s from a height of 110 m above ground level (AGL). It took around 25 min to complete the plan and collected 291,695 frames in total. Frames from 95000 to 245999 belonged to the site. The area is around 13.8 ha, which could cover 1186 pixels in Sentinel 2 image and 113 pixels in Landsat 8 image. To consider illumination changes, we measured irradiance before and after the flight. irradiance was interpolated to each image frame and gaussian convoluted to Headwall wavelength.

Sensor	Spectral region	Bands	FWHM	AFOV (°)
Headwall Nano	400 ~ 1000 nm	273	6 nm	21.1
ASD FieldSpec4	350 ~ 2500 nm	2151	3 nm at 700nm	25
			10 nm at 1400 nm	
			10 nm at 2100 nm	

Table 1 Sensor overview

2.3   Data processing

Drone Hyperspectral Data Processing

Sensor Calibration $\longrightarrow$ BRF Calculation $\longrightarrow$ Spectral Aggregation $\longrightarrow$ NBAR Normalization

Orthorectification $\longrightarrow$ **Co-registration** $\longrightarrow$ Spatial Aggregation $\longrightarrow$ Quality Assessment

Satellite Dataset

Level 2 Product $\longrightarrow$ Quality Check $\longrightarrow$ BRF Conversion $\longrightarrow$ NBAR Normalization
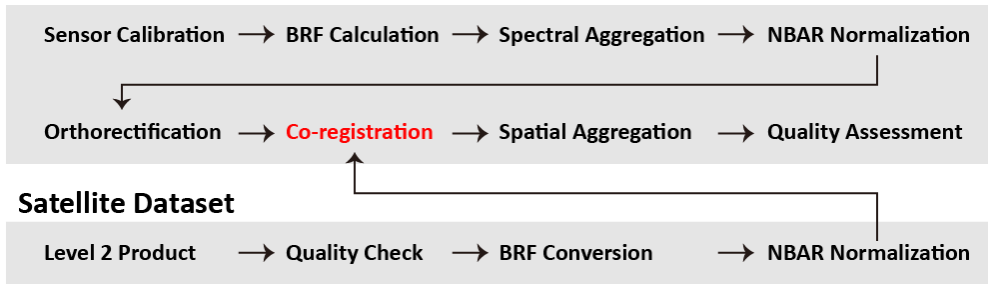
Figure 2 Data processing overview

Element	Peak wavelength (nm)
Hb, Fe	486.13
Mg, Fe	516.73
Na	589.1
Ha	656.3
O_2-B	686.85
O_2-A	760.41
Ca II	854.25
Water vapor	866.24

Table 2 Reference Fraunhofer lines from (Busetto et al., 2011; Meroni et al., 2010).

2.3.1 Sensor calibration
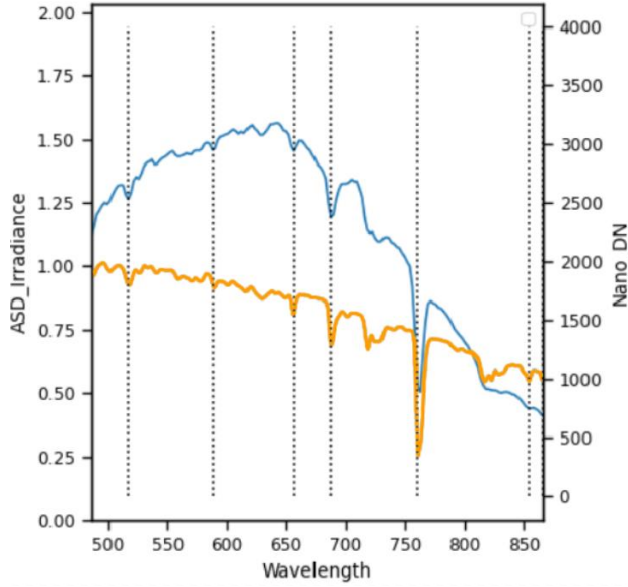
Figure 3 Wavelength calibration: the orange line represents the irradiance measured by ASD FieldSpec4 (ASD_Irradiance) and the blue line represents the averaged white frames by Headwall Nano (Nano_DN). The dotted lines indicate the Fraunhofer lines (Table 2)

The calibration consisted of wavelength calibration and radiometric cross-calibration. For the wavelength calibration, we referred to 8 Fraunhofer lines and matched them to corresponding peak bands from the white frame (Table 2) (Busetto et al., 2011; Meroni et al., 2010; headwall review paper). 1st order linear regression determined the wavelength of each band. For the radiometric calibration, we referred to the observed irradiance and determined the radiometric calibration matrix (Eq 1).

$$R_{ij} = \pi \frac{(White_{ij} - Dark_{ij})}{IRR} \ (i = 1 \sim 640; j = 1 \sim 273) \qquad \textbf{Eq 1}$$

The radiometric calibration was carried out pixel by pixel. The variable i and j indicate the pixel and band number. R, white, and Dark represent the radiometric calibration matrix of Headwall Nano, the averaged white frame and dark frame. They are made up of 640 by 273 matrix. For example, R_{ij} indicates the radiometric calibration coefficient in the i th pixel and the j th band. IRR is the irradiance observed in parallel with white frames. In this case, we used observed irradiance instead of simulated one.

6

2.3.2   Bidirectional reflectance factor (BRF) calculation

As a single spatial pixel has very narrow AFOV, the reflectance was assumed to BRF. it was computed from raw DN. At first, digital number (DN) was converted to radiance by the radiometric calibration factor (Eq 2).

$$\text{Rad}_{ijk} = R_{ij}(DN_{ijk} - Dark_{ij}) \ (i = 1 \sim 640; j = 1 \sim 273) \qquad \textbf{Eq 2}$$

The variable i, j and k indicate the pixel, band and frame number. The image frames from 95000 to 245999 belongs to the study site so k ranges from 95000 to 245999. Rad and DN represent radiance and digital number. R and Dark are the radiometric calibration matrix and the dark frame. The same values of R and Dark were applied to the whole image frames. Then, BRF was rescaled by irradiance (Eq 3). Later, the hyperspectral BRF is aggregated to multispectral by the spectral response function (Table 5).

$$\text{BRF}_{ijk} = \pi \frac{Rad_{ij}}{IRR_{ik}} \ (i = 1 \sim 640; j = 1 \sim 273; k = 95000 \sim 245999) \quad \textbf{Eq 3}$$

BRF, Rad and IRR represent BRF, radiance and the simulated irradiance, respectively. The same irradiance was applied to the corresponding frame.

2.3.3   BRDF correction

To unify sensor geometry between drone and satellites, drone HSI was normalized to nadir BRDF adjusted reflectance (NBAR) by the BRDF normalization technique (Claverie et al., 2015; Roy et al., 2017a; Roy et al., 2017b; Roy et al., 2016a). It was originally designed for Landsat and Sentinel 2, BRDF of which cannot be retrieved internally. It refers to a BRDF model, Ross-Thick-Li-Sparse (RTLS) model. Assuming the global mean BRDF shape, 3 model parameters, isometric, volumetric and geometric scattering coefficient, are retrieved from the MODIS BRDF product (Table 3). In spite of limitations, the BRDF normalization method shows reliable results and widely used in Landsat 8 and Sentinel 2. To be consistent with satellites, the same method was applied to drone BRF map.

Bands	Isotropic	Volumetric	Geometric
Blue	0.0774	0.0372	0.0079
Green	0.1306	0.0580	0.0178
Red	0.1690	0.0574	0.0227
RedEdge1	0.3093	0.1535	0.0330
RedEdge2	0.2316	0.1003	0.0273
RedEdge3	0.2599	0.1197	0.0294

NIR	0.3093	0.1535	0.0330

Table 3 MODIS global mean BRDF parameters from (Roy et al., 2017a; Roy et al., 2017b)

2.3.4 Orthorectification

The orthorectification consists of 4 steps: the retrieval of pixel viewing geometry, the retrieval of height, reprojection and aggregation. Pixel viewing geometry is defined by a unit vector where a pixel is headed in the world coordinate. In the image coordinate, the pixel vector was retrieved from the sensor geometry. Then, it was converted to the world coordinate. Sensor geometry was acquired from global positioning system and inertia navigation system (GPS/INS), which is attached to Headwall Nano. They record latitude, longitude, altitude, roll, pitch, yaw and time with 5 ms interval. Due to the mismatch in sampling frequency between the GPS/INS and the imager, the GPS/INS samples were linearly interpolated to image frames. Pixel vectors were defined by (Eq 4) and then converted to the world coordinates by rotation matrix (Eq 5 and Eq 6) (Jia et al., 2020).

$$\begin{bmatrix} x \\ y \\ z \end{bmatrix} = \begin{bmatrix} \cos(t) & 0 & \sin(t) \\ 0 & 1 & 0 \\ -\sin(t) & 0 & \cos(t) \end{bmatrix} \begin{bmatrix} 0 \\ 0 \\ -1 \end{bmatrix}, t \in [-10.5, 10.5 \, deg] \qquad \textbf{Eq 4}$$

$\begin{bmatrix} x \\ y \\ z \end{bmatrix}$ and $\begin{bmatrix} X \\ Y \\ Z \end{bmatrix}$ represent a pixel vector in the image coordinate and the world coordinate. $\begin{bmatrix} 0 \\ 0 \\ -1 \end{bmatrix}$ indicates the nadir vector. As a push broom sensor, Headwall scans frames perpendicular to the along-track, which accords with the roll axis. Rotating the nadir vector within the 21.1 deg of AFOV, pixel vectors were defined.

$$\begin{bmatrix} X \\ Y \\ Z \end{bmatrix} = Rot \begin{bmatrix} x \\ y \\ z \end{bmatrix} \qquad \textbf{Eq 5}$$

$$Rot = \begin{bmatrix} \cos(w) & -\sin(w) & 0 \\ \sin(w) & \cos(w) & 0 \\ 0 & 0 & 1 \end{bmatrix} \begin{bmatrix} \cos(r) & 0 & \sin(r) \\ 0 & 1 & 0 \\ -\sin(r) & 0 & \cos(r) \end{bmatrix} \begin{bmatrix} 1 & 0 & 0 \\ 0 & \cos(p) & -\sin(p) \\ 0 & \sin(p) & \cos(p) \end{bmatrix}$$

$$\textbf{Eq 6}$$

p, r and w indicate the pitch, roll and yaw of a frame. Rot represents a rotation matrix. It is made up of successive rotations on the pitch, roll and yaw axis. By

multiplying the rotation matrix by the pixel vector in the image coordinate, it is converted to the world coordinate. To determine the exact geocoordinate from the vector, its elevation is required in prior (Eq 7).

$$\begin{bmatrix} X' \\ Y' \\ Z' \end{bmatrix} = \begin{bmatrix} X \\ Y \\ Z \end{bmatrix} * \frac{Alt - H}{Z} \qquad \text{Eq 7}$$

$$Merit(h) = \left(\begin{bmatrix} X'_1 \\ Y'_1 \\ Z'_1 \end{bmatrix} - \begin{bmatrix} X'_2 \\ Y'_2 \\ Z'_2 \end{bmatrix} \right)^2 \quad (h \in [180, 220]) \qquad \text{Eq 8}$$

$\begin{bmatrix} X' \\ Y' \\ Z' \end{bmatrix}$ represents the pixel geocoordinate: UTM x, UTM y and altitude, respectively.

Alt is the altitude recorded by GPS/INS and H is the estimated altitude. Lacking of a fine scale digital elevation model (DEM), we estimate the elevation from the overlapped scene between flight lines. From the scene, we matched pairs of identical points and determined the altitudes by minimizing a merit function. The pairs were extracted and matched by a computer vision algorithm, SURF (Speeded Up Robust Features) (Angel et al., 2020; Habib et al., 2016; Bay et al., 2008). The merit function is defined by the distance between a pair of geocoordinates: $\begin{bmatrix} X'_1 \\ Y'_1 \\ Z'_1 \end{bmatrix}$

and $\begin{bmatrix} X'_2 \\ Y'_2 \\ Z'_2 \end{bmatrix}$. The two are computed by (Eq 7) at an altitude of h. Varying h from 180 to 220 m, we estimate the altitude minimizing the merit function (Eq 8). Referring to the altitude on the matched points, we interpolated and extrapolated them to the whole pixels: bilinear interpolation and nearest neighbor extrapolation was applied. After DSM was estimated, pixel vectors were orthorectified (Eq 7).

2.3.5 Spatial Aggregation

Figure 4 Spatial aggregation of drone HSI to satellite scale. The left images are satellite SR: Landsat 8 and Sentinel 2B. The red square indicates the region of interest. The right images are drone HSI. The white grid lines are identical to corresponding satellite grid cells. On Sentinel 2 image, our site is located on the backward scattering region. On Landsat 8 image, our site is located on the forward scattering region.

Not to lose the spatial benefit, HSI was aggregated at 50 cm level. After co-aligned to the satellite HSI, it was aggregated to the satellite scale again. Referring to the satellite UTM grid, the BRF points were averaged within the corresponding squared pixel.

2.3.6 Co-registration

Sentinel 2 and Landsat 8 are reported to have the geographical displacement, which sometimes exceeds the unit pixel (Yan et al., 2016). To co-align images, we apply the automated scene co-registration technique (Houborg & McCabe, 2018). In doing so, NDVI images were used. Referring satellite NDVI image as a base image, it optimizes the pixel shifts on drone NDVI image by maximizing the spatial autocorrelation (S4 and S5).

2.4 Satellite dataset

Platform	Acquisition time (UTC + 9:00)	SAA	VZA	Cross-track

Landsat 8	2020-10-05 11:10	156°	3.0°	98.2°
Drone	2020-10-07 10:42	147°	-10 ~ 10°	30°
Sentinel 2B	2020-10-09 11:16	159°	-2.5°	98.62°

Table 4 Sensor geometry. SAA and VZA indicates solar zenith angle and view zenith angle, where the satellites or drone observes our study area.

Platform	Channel (Band number)	Pixel size (m)	Central Wavelength (nm)	Band width (nm)
Sentinel 2B	Blue (band 2)	10	490	65
	Green (band 3)	10	560	35
	Red (band 4)	10	665	30
	Red Edge1 (band 5)	20	705	15
	Red Edge2 (band 6)	20	740	15
	Red Edge3 (band 7)	20	783	20
	NIR (band 8)	10	842	115
	Narrow NIR (band 8A)	20	865	20
Landsat 8	Blue (band 2)	30	480	60
	Green (band 3)	30	560	60
	Red (band 4)	30	655	30
	NIR (band 5)	30	865	30

Table 5 Band configuration in Sentinel 2B and Landsat 8 (Drusch et al., 2012; Roy et al., 2014).

2.4.1 Sentinel 2B

We introduce the Sentinel 2 SR products: 10 m and 20 m. Sentinel 2 observes land surface within an AFOV of 20.6° (Roy et al., 2017b). The 10 m product consists of 4 bands (Table 5): Blue, Green, Red and NIR. The spectral configuration of 3 visible bands approximates to the Landsat 8. The NIR represents typical broad NIR, which is close to that of Landsat 7. The 20 m product consists of 7 bands (Table 5): Blue,

Green, Red, Red Edges (RedEdge1, RedEdge2 and RedEdge3) and narrow NIR. The 3 visible bands are resampled from the Level 1B product so identical to those in 10 m product. Narrow NIR differs in band width as well as spatial resolution from NIR. It represents narrower NIR, which is close to that of Landsat 8. After projected by B-spline interpolation, Sentinel 2 level 2 products are atmospherically corrected by Sen2Cor. Sentinel 2 provides cloud mask at 20 m scale. However, it sometimes fails to distinguish clouds from bright land surface (Frantz et al., 2018). The cloud mask recognized a small rice paddy and a building roof top as clouds, which are clearly identifiable in visual inspection. Due to the unreasonable performance, we used Fmask instead (Claverie et al., 2018). All the pixels belonging to our site were marked as clear. The Sentinel 2B level 2 products were downloaded from Copernicus open access hub (https://scihub.copernicus.eu/).

2.4.2 Landsat 8

We introduce the Landsat 8 level 2 SR products. Landsat 8 observes land surface within an AFOV of 15° (Roy et al., 2014). We targeted the VNIR band: Blue, Green, Red and NIR (Table 5). They all have 30 m resolution. As mentioned in (Section 2.4.1.), they are close to Blue, Green Red and narrow NIR in Sentinel 2, respectively. After projected by cubic interpolation, Landsat level 2 product is atmospherically corrected by LaSRC (Roy et al., 2014). Landsat 8 provides quality assessment band and all the pixels belonging to our site were marked as clear: 2720, 2724, 2728 and 2732. The Landsat 8 level 2 SR product was downloaded from USGS (https://earthexplorer.usgs.gov/).

Chapter 3. Result and Discussion

3.1 Drone HSI quality assessment

3.1.1 Radiometric accuracy

To validate the radiometric accuracy of our drone HSI, we compared on-flight to ground level radiance on the same target. We set the 99% Spectralon as the reference due to the Lambertian characteristic and the higher reflectivity. The radiometric accuracy was assessed by means of spectral similarity and residual error. To verify the overall similarity in spectral shape, spectral angle (SA) and determinant of coefficient (R^2) were calculated between each validation set (Tan et al, 2020). For residual error, normalized root mean squared error (NRMSE) was calculated by wavelength (Hakala et al., 2018).

$$SA\ (°) = \arccos\left(\frac{\vec{x}\cdot\vec{y}}{\|\vec{x}\|\|\vec{y}\|}\right) \qquad\qquad \textbf{Eq 9}$$

$$NRMSE\ (\%) = \frac{E((\vec{x}-\vec{y})^2)}{E(\vec{y})} * 100 \qquad\qquad \textbf{Eq 10}$$

where $\vec{x}$ and $\vec{y}$ indicate on-flight and ground radiance, respectively (Eq 9 and 10).

18 Spectralon scenes were acquired in total. To be sure of the radiometric uniformity, coefficient of variation (CV) was calculated among 3 * 3 pixels on the Spectralon pixels and we discarded non-uniformed pixels (S2). To avoid adjacency effect, only the center pixel on the Spectralon is selected. We continuously measured irradiance from 9 am to 2 pm with 10-second interval. Due to the Lambertian characteristic, the ground level radiance is calculated by irradiance/π (Schaepman-Strub et al., 2006). We discarded the ground reference under unstable atmospheric condition. Finally, we paired 8 on-flight Spectralon pixels with the corresponding ground level radiance.
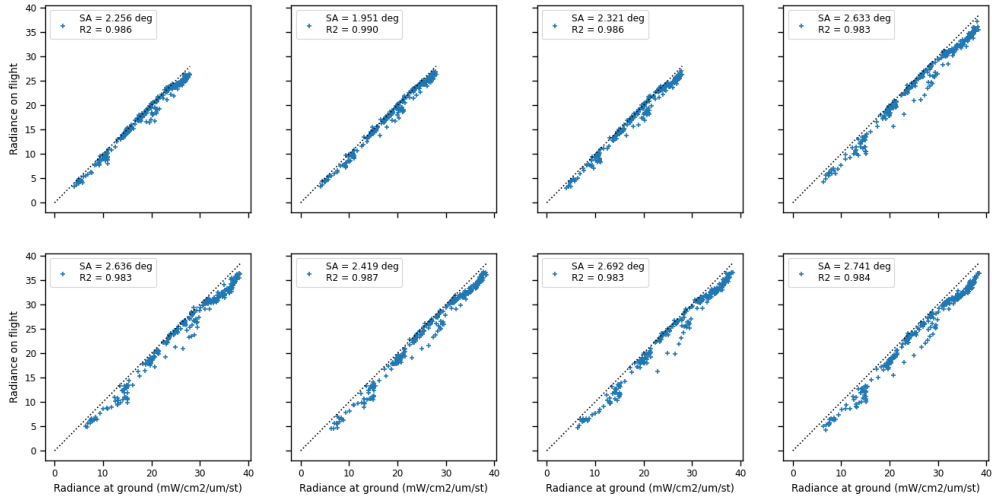
Figure 5 the consistency between ground and on-flight radiance.

For the 8 validation sets, on-flight radiance shows good agreement with ground references. Figure 5 illustrates scatter plots of on-flight radiance versus ground reference. The first three on the first column were measured around 9:00 am and the others were measured around 10:00 am. Due to difference illumination condition, the radiance value differed (S1). Most points are aligned with 1:1 line (dotted line), but on-flight observations slightly underestimated the higher radiance. Still, SA ranges from 1.95° to 2.741° and R^2 is about 0.98. The statistics are also

comparable with (Tan et al., 2020), which reported 3° of SA and 0.98 of R^2 on soils and vegetation plots.
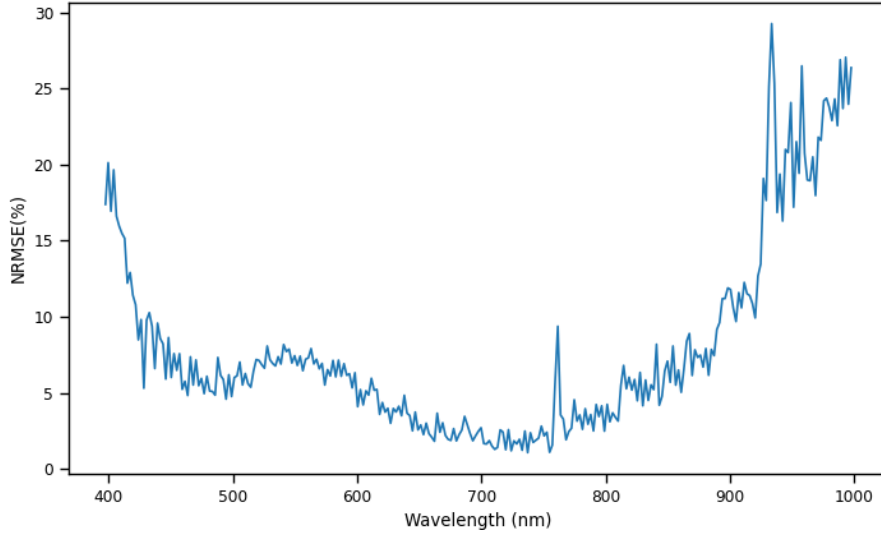
Figure 6 The accuracy of radiometric calibration by wavelength.

Figure 6 illustrates NRMSE by wavelengths, integrating all the 8 validation sets. Due to atmospheric absorption (i.e. oxygen or water vapor) and low signal to noise ratio, the NRMSE was higher on the region below 420 nm, over 900 nm or O2A band (near 761 nm). Except these regions, the overall NRMSE was below 8 %. On the visible region, the NRMSE was slightly higher than expected. Although only the central pixel was extracted, the sensor point spread function (PSF) might cause adjacent effect. During the field campaign, the Spectralon was put on the sponge cover for possible damage. The cover has very low reflectivity on visible region so the adjacent effect appeared evidently (S3). It also resulted in the relatively higher CV (S1). Despite possible errors in the validation (i.e. PSF), the 8 % of NRMSE is comparable with (Hakala et al., 2018), which reported 7.6% of calibration error.

Due to low altitude, atmospheric correction was not conducted in this study (Kwon et al., 2020; Hakala et al., 2018; Adão et al., 2017). Though, radiometric accuracy was reliable by means of spectral shape and residual error. The statistics are also comparable with other vicarious calibration studies (Tan et al., 2020; Hakala et al., 2018). We noticed a possible error source (the sensor PSF), but the spectral and spatial aggregation is supposed to alleviate it (**2.3.2.** and **2.3.5.**). We concluded that atmospheric effects and sensor PSF are negligible and our drone HSI assures the qualitative radiometric accuracy.

3.1.2 BRDF effect

Harvested cropland mainly covers our site and less BRDF effect is expected accordingly (Roy et al., 2016c; Franch et al., 2013; Vermote et al., 2009). Figure 7 and 8 show BRDF effect on the study site before and after BRDF normalization, respectively. Following the method described in (Roy et al., 2016b), reflectance differences were calculated on overlapped swaths and scattered by view zenith angle (VZA). Overall BRDF effect was quantified by regression slope and B-F. B-F is the average difference between reflectance on backward and forward scattering region within the sensor geometry (Roy et al., 2016c). Regardless of BRDF normalization, the statistics were sustained with a tiny value: -0.0001 of slope and 0.004 of B-F. Although this site shows less BRDF effect, we applied BRDF normalization to our drone HSI for two reasons. First, sensor viewing geometry also induces BRDF effect and our sensor has larger AFOV than the satellites. As Adão et al. (2017) noticed, it is not negligible in general. Second, map to map comparison is based on the accordance of viewing geometry between two maps (Claverie et al., 2015). In doing so, BRDF normalization conceptually unifies the geometries.
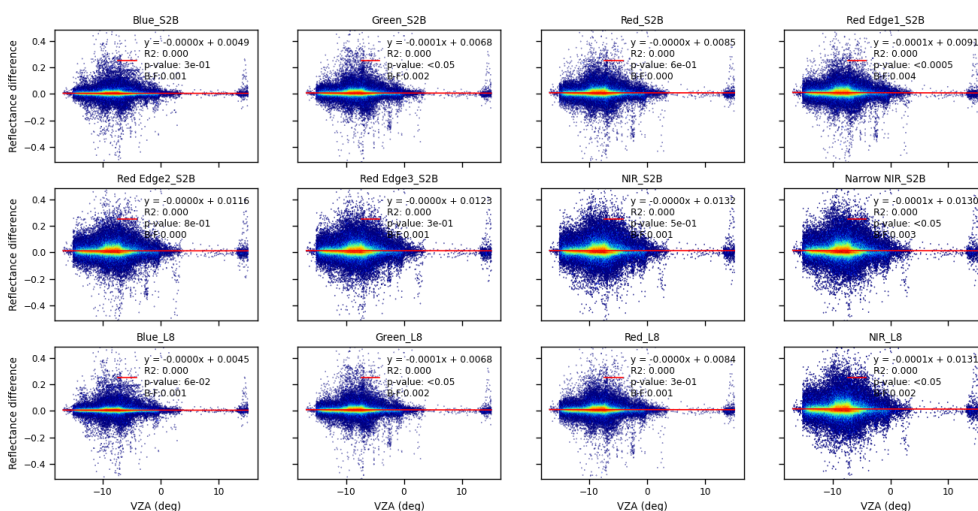
Figure 7 BRDF effect before BRDF normalization. Each subplot indicates spectrally aggregated bands: the first and second columns (S2B) by Sentinel 2B SRF and the last one (L8) by Landsat 8 SRF. Following (Roy et al., 2016b), reflectance differences were quantified and scattered by view zenith angle (VZA) of reference flight lines. Each point represents the reflectance pair where the one headed forward scattering region and the other one headed backward scattering region.
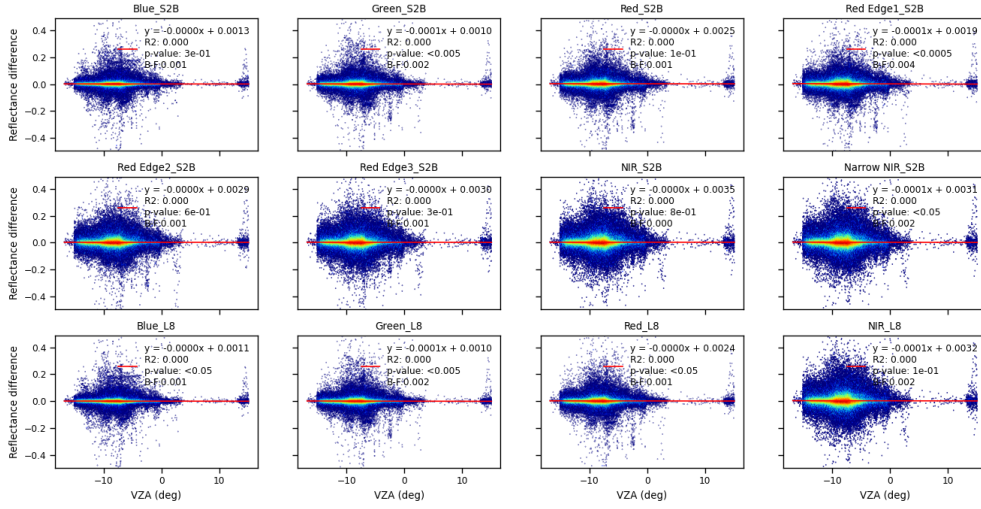
Figure 8 The same as Figure 7, but after BRDF normalization.

3.2 Spatial variability in satellite surface reflectance product

To evaluate satellite SR, we compared it to drone BRF map, pixel by pixel. The assessment was performed by ordinary linear regression and the statistical matrix, called APU matrix: x, y and N indicate NBAR in satellite, drone map and the number of samples, respectively (Eq 11, 12 and 13). Suggested by Vermote et al. (2008), APU matrix is commonly used in satellite SR evaluation studies (Vermote et al., 2016; Clavarie et al., 2015; Clavarie et al., Doxani et al., 2018). It consists of Accuracy (A), Precision (P) and Uncertainty (U). A, P and U quantify mean bias error, standard deviation of error and root mean squared deviation, respectively. The quality of satellite NBAR was analyzed by theoretical error budget. Theoretical error budget is the uncertainty in atmospheric correction. Simulating 6S, Vermote et al. (2008) quantified the uncertainty: 0.005 + 0.05*SR for SR and 0.02 + 0.02*VI for VI. If the absolute difference between a value and the reference value fell within the theoretical error budget, it is considered as good (Vermote et al., 2008).

$$A = \frac{\sum(x-y)}{N} \qquad\qquad \textbf{Eq 11}$$

$$P^2 = \frac{\sum(x-y-A)^2}{N-1} \qquad\qquad \textbf{Eq 12}$$

$$U^2 = \frac{\sum(x-y)^2}{N} \qquad\qquad \textbf{Eq 13}$$

Within the study area, all the pixels in Sentinel 2B and Landsat 8 SR are marked as clear pixel: 1,178 pixels for the Sentinel 2B 10 m product, 271 pixels for the Sentinel 2B 20 m product and 111 pixels for the Landsat 8 product. The evaluation was carried out by comparing them to corresponding pixels on drone NBAR.

3.2.1 Sentinel 2B (10m)
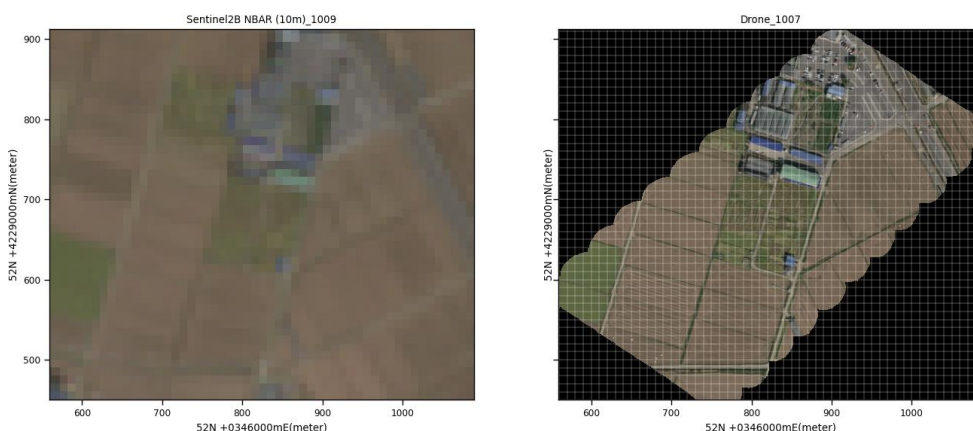
Figure 9 Study site and spatial gridding. The left one is the Sentinel 2B RGB image and the right one is our drone RGB image. On the right image, white gridding lines indicate the corresponding pixels on the Sentinel 2B image.
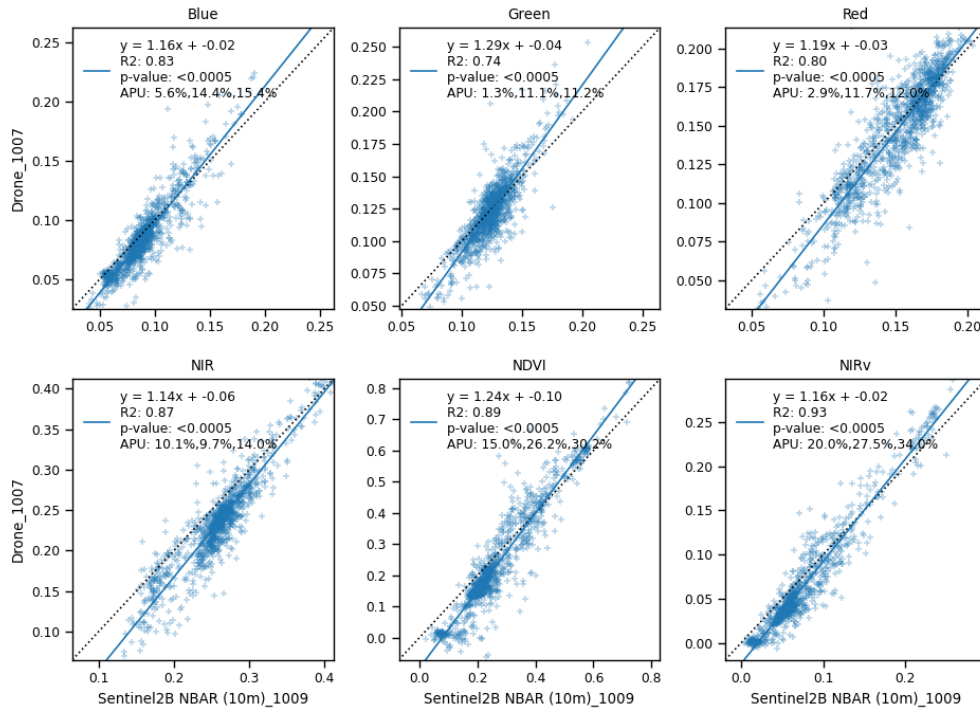
Figure 10 Scatter plot of Sentinel 2B NBAR (10 m) versus drone NBAR. Each subplot represents bands or VIs. Blue line indicates the regression line. APU describes A, P and U value in percentages.

Figure 10 shows the scatter plots of Sentinel 2B NBAR (10m) versus drone NBAR. Each subplot represents bands or vegetation indices. For VNIR, the regression slopes are all positive: 1.16 (Blue), 1.29 (Green), 1.19 (Red) and 1.14 (NIR). Darker pixels were overestimated while brighter pixels were underestimated on Sentinel 2B NBAR (10m). It implies that the path radiance was under-corrected. As for VIS, the shorter wavelength bands are strongly affected by aerosols. Dispersing outgoing radiance, it makes brighter pixels darker and darker pixels brighter. On the study area, Sentinel 2 retrieved AOT by 0.1. Although Sen2Cor tends to overestimate AOT, the deviation was higher at the lower AOT (Li et al., 2018; Pflug et al., 2014). The positive slope indicates that the AOT was underestimated.

Sentinel 2 NBAR (10m) tends to overestimate the SR by means of A: 5.6% (Blue), 1.3% (Green), 2.9% (Red) and 10.1% (NIR). The VIS shows good agreement with drone NBAR. Due to the lower signal, aerosol contamination was evident on Blue, A of which is slightly higher than the absolute radiometric uncertainty of 5% (Gascon et al., 2017). On the contrary to VIS, NIR looks biased, A of which is almost

doubled than the Blue. It relates to the worse performance of Sen2Cor on infrared bands (Doxani et al., 2018). With a lower P and higher R^2, the additional linear correction is recommended.
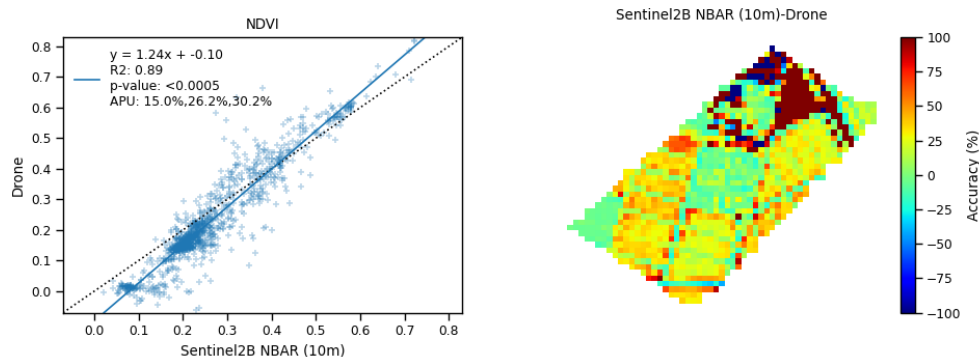
Figure 11 Scatter plot and accuracy map of Sentinel 2B NBAR (10 m) versus drone NBAR. The left one is the same as Figure 10 but only for NDVI. The right one illustrates the spatial distribution of the accuracy.
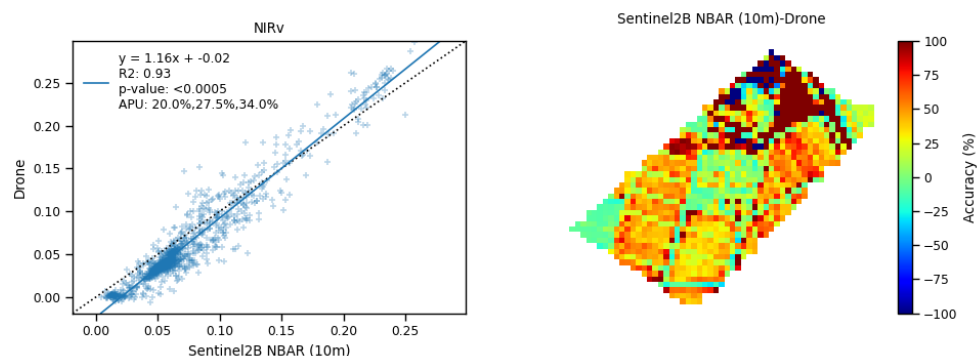
Figure 12 The same as Figure 11 but for NIRv.

Due to the higher bias in NIR, NIR based VIs might be as well: 15.0% (NDVI) and 20.0% (NIRv). The extreme bias, however, stems from the nature of the dividing equation. NDVI is a vegetation index normalized by (NIR + Red). The equation itself is extremely noisy to targets which of both NIR and Red value are low (S4), such as concretes. The biased pixels in VIs are concentrated to northern parking lot (Figure 11 and 12). The A exceeds 100%.
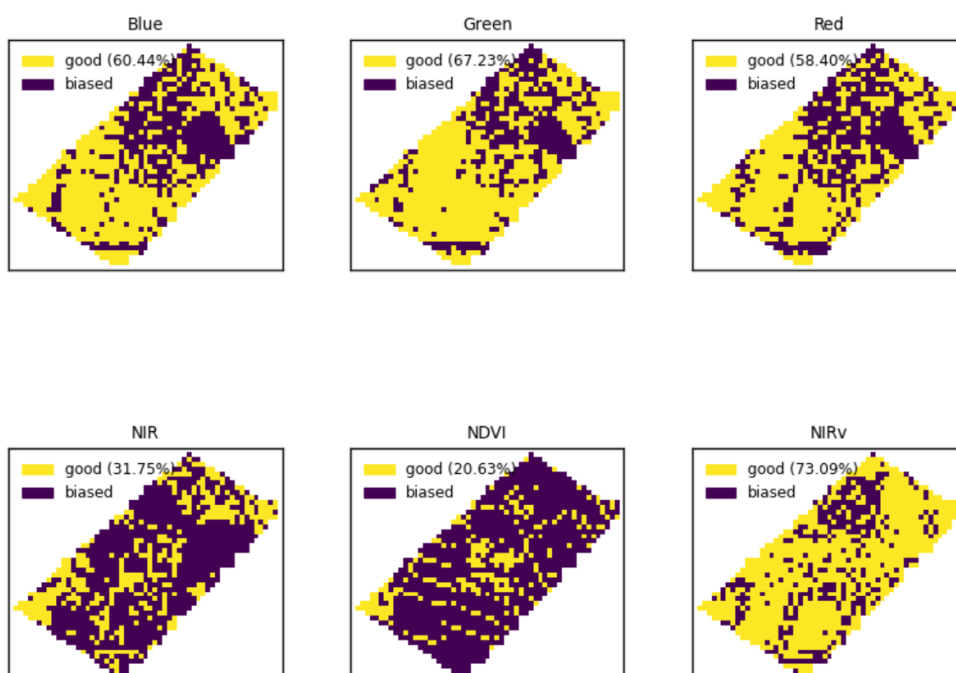
Figure 13 The quality maps illustrate the spatial pattern of "good" pixels on Sentinel 2 NBAR (10m). Each subplot represents the band. Yellow pixels are marked as "good" while purple pixels are biased.
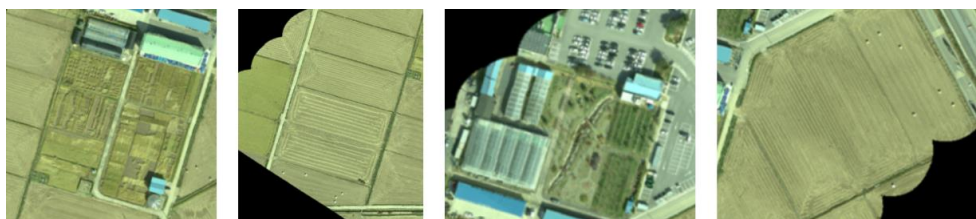
Figure 14 From left to right, they correspond to the sparsely vegetated area (center), narrow roads (south and west), built-in area (north) and eastern two rice paddies, respectively. Except the built-in area scene, the other scenes include the plants between rice paddies.

Figure 13 shows the spatial distribution of good pixels and the proportion (Q) on Sentinel 2B NBAR (10m). The Q is much higher on VIS than on NIR: 60.44% (Blue), 67.23% (Green), 58.40% (Red) and 31.75% (NIR). For VIS, biased pixels are distributed over 4 areas: the roads (south and west), sparsely vegetated area (center), built-in area (north), and the two eastern harvested area (Figure 14). The roads are narrower than a unit pixel and located between two rice paddies. Similarly,

the sparsely vegetated area shows the higher heterogeneity by soils and rice. The contrast in reflectance increases the heterogeneity in a pixel. On satellite images, a pixel is affected by the surrounding pixels and the influence can be described as a PSF. Sentinel 2 10m bands has the PSF which of FWHM is around 22m (Radoux et al., 2018). Due to the wider FWHM than a 10m pixel, Sentinel 2B NBAR (10m) fails to distinguish the finer mixture from the adjacent pixels.

Only SR could not track fine scale dynamic in spite of the pixel size. Built-in area consists of cars and glossy rooftop. Cars are the similar case to the sparsely vegetated area. Glossy rooftop shows extreme BRDF effect: within the FOV, the reflectance varies by 0.2 NIR (S5). For the extreme target, the MODIS global parameter seems not working properly. The trickiest bias occurred on the two eastern harvested area: the purple and triangular area. The eastside edge is not perpendicular to the drone flight line so the bias should not relate to BRDF effect (Figure 1). It is not parallel to the drone flight line so the bias should not relate to the sensor calibration or irradiance changes. Rather the edge accords to the boundary between rice paddies. On the Figure 14, the rightmost scene shows 3 rice paddies: the right paddy was classified as good while the others were overestimated. On the right paddy, straws were collected and bailed for the silage (6 white dots). On the other 2 paddies, straws were remained. It seems the surface changed for 2 days. On Oct 7th (drone campaign), straws were remained so the structure shaded the surface. After 2 days (Sentinel 2 overpassing), the baling was preceded so the shadow disappeared. The surface structure change could significantly affect reflectance. Except for that, the bias by the other possible surface change fell within the theoretical error budget, including vegetated areas: rice paddies (south west) and park (north) (Figure 1). Within a short period, the surface change seems not exceeding the atmospheric correction error.

A few pixels were classified as good on NIR. Vegetated areas account for good quality pixels, but the spatial distribution is not clear. The higher A in NIR is expected to affect the quality map for VIs. The Q in the VIs differs: 20.63% (NDVI) and 73.09% (NIRv). Overall, the NDVI seems biased. However, the spatial pattern obviously represents a vegetated area. The sparsely vegetated area on the center and the plant between rice paddies are evidently identifiable. Despite the bias in NIR, the sensitivity of NDVI to absorbed photosynthetically activate radiation results in the good agreement on vegetated areas (Huete et al., 1997). Similarly, Radoux et al. (2016) demonstrated that NDVI could distinguish plants from mixed pixels, even though the plant occupies less than 10% of the pixel. Interestingly, the good quality in reflectance measurement does not guarantee the good quality in NDVI. The north

part was classified as good on both the Red and the NIR, but resulted in biased NDVI. As already noticed, it stems from the nature of the equation (S4). On the contrary to the NDVI, the NIRv looks better than the reflectance. Only the wide PSF blurs the narrow roads and built-in area. However, the NIRv does not captured the structural change (the eastern two harvested area; Figure 14). Multiplied by NIR to NDVI, NIRv seems regulated by NIR. Although NIR was biased, the lax criterion for VI makes specious result. To guarantee the consistency between in-situ to satellite observation, the current linear quality threshold (0.2 + 0.2*VI) fails to track the non-linearity of VIs. Our result implies that VI should be comprehended by the equation itself as well as the physical meaning.

Sentinel2	Satellite SR vs Drone NBAR				Satellite NBAR vs Drone NBAR			
(10m)	A (%)	P (%)	U (%)	Q (%)	A (%)	P (%)	U (%)	Q (%)
Blue	7.2	14.2	16.0	57.47	5.6	14.4	15.4	60.44
Green	3.0	11.0	11.4	66.04	1.3	11.1	11.2	67.23
Red	4.4	11.6	12.4	55.94	2.9	11.7	12.0	58.40
NIR	11.8	9.6	15.2	23.68	10.1	9.7	14.0	31.75
NDVI	15.1	26.2	30.3	20.46	15.0	26.2	30.2	20.63
NIRv	21.9	27.0	34.8	71.14	20.0	27.5	34.0	73.09

Table 6 The summary of APU matrix and the Q on Sentinel 2 SR (10m) and NBAR (10m). A, P and U indicate accuracy, precision and uncertainty by percentage. The right 4 rows organize the statistics in Figure 10 and Figure 13.

Table 6 summarizes APU matrix and Q of qualified pixels of Sentinel 2 SR before and after BRDF normalization. Sentinel 2 observed our study area with a VZA of -2.5° and a RAA of 60° (Table 4). The VZA approximates to nadir and RAA is also close to orthogonal plane. Overall SR should be overestimated a little bit. Without exception, BRDF normalization improved the A by around 2 %. Q also increased by 3 ~ 7%, but the spatial pattern of good pixels is almost sustained (Data not shown). For example, the biased band NIR shows a specious improvement in the A and Q. The spatial pattern of qualified pixels, however, is far from the other unbiased bands (Figure 13 and 14). Despite BRDF normalization, the NIR is misguided. Although some studies noted the BRDF effects on Sentinel 2, our result implies that the bias in atmospheric correction overwhelms BRDF effect (Roy et al., 2017a; Roy et al., 2017b).

3.2.2 Sentinel 2B (20m)
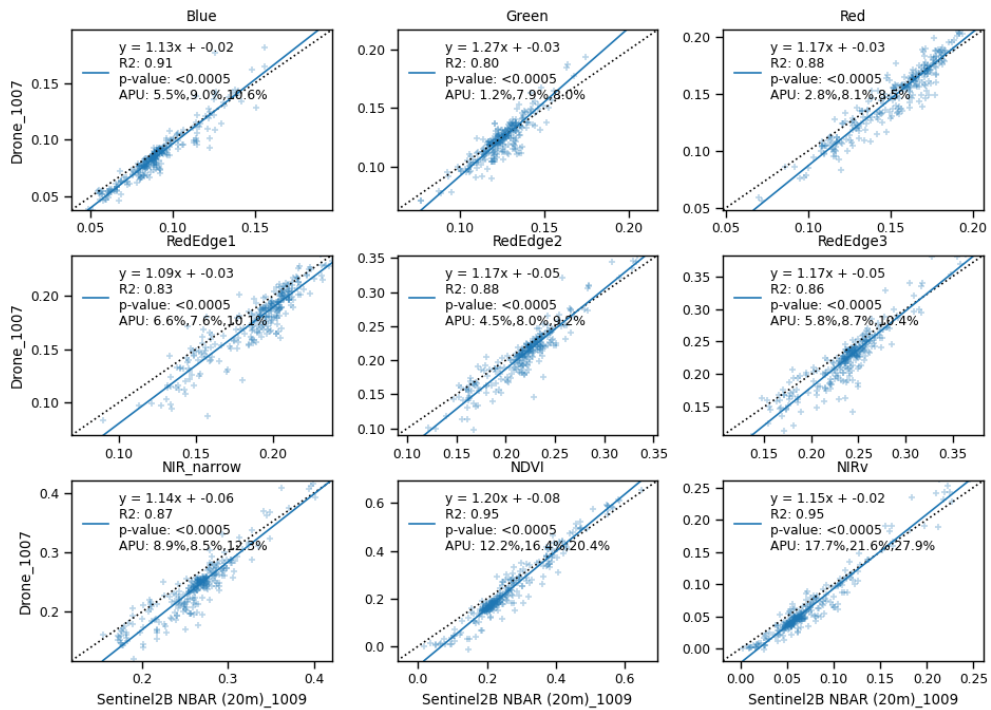
Figure 15 The same as Figure 10 but for Sentinel 2B NBAR (20m).

Figure 15 and 16 illustrate the same as Figure 10 and 13, respectively, but for the 20m bands. Except narrow NIR, Sentinel 2 20m bands show good agreement. VIS bands show similar results to the 10 m bands with the A and P improved. The A of Blue exceeds 5%, but the Q is comparable with the Green and the Red: 71.96% (Blue), 80.81% (Green) and 71.96% (Red). The slightly higher bias should stem from the land surface change (3.2.1.). Likewise, Red edge 1 and 3 bands seemed biased, but the spatial pattern of good pixels are similar to the VIS (Figure 16). Sen2Cor algorithm reported to be biased over infrared bands, the Q is lower than the VIS (Doxani et al., 2018): 59.04% (Red edge 1), 64.58% (Red edge 2) and 58.30% (Red edge 3). The narrow NIR, meanwhile, does not show any spatial pattern and the overall A indicates the biased reflectance, accordingly.
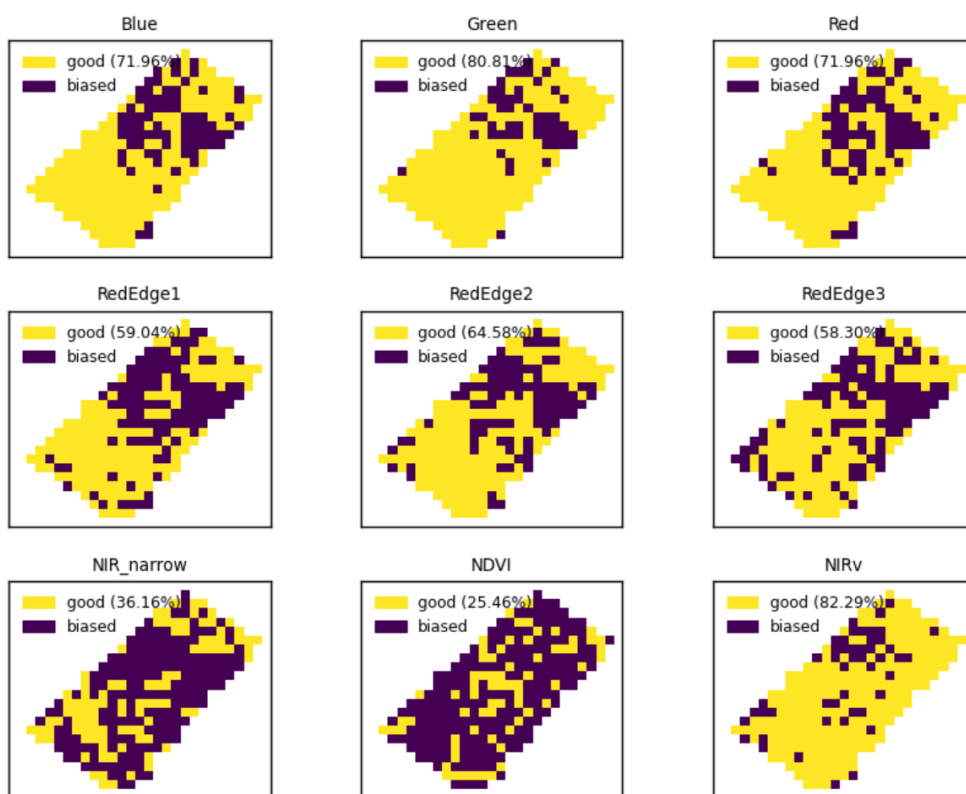
Figure 16 The same as Figure 13 but for Sentinel 2 NBAR (20m).
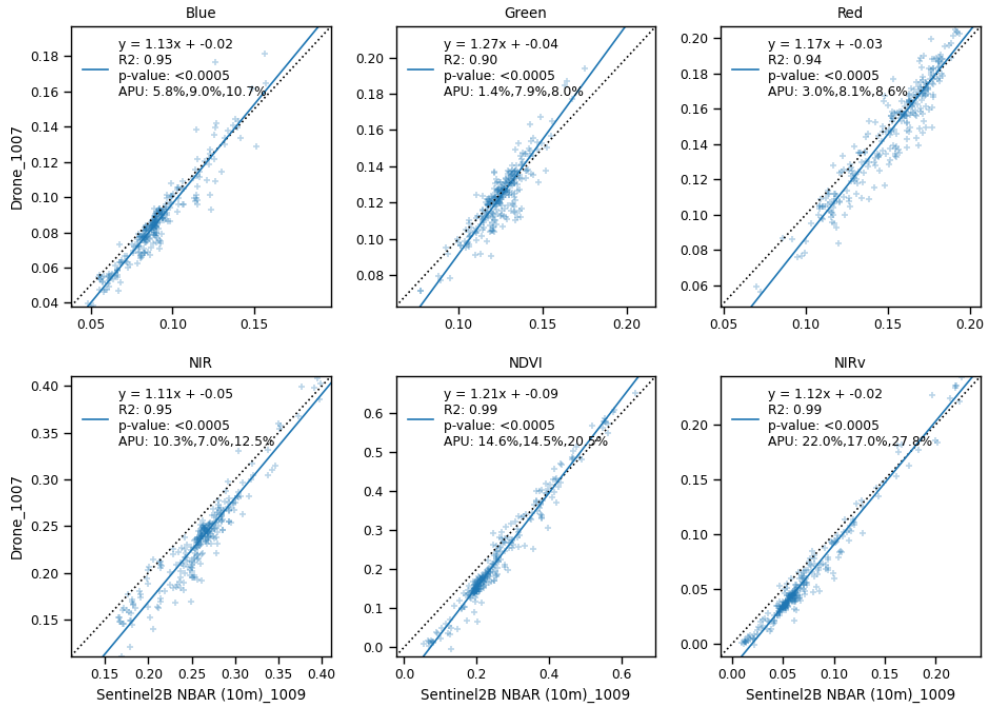
Figure 17 The same as Figure 10 but the 10m bands were aggregated to 20m scale.

The VIS on 20m bands are consistent with the 10m bands but bilinearly resampled from the level 1B. Comparing to the 10m bands, the regression slopes get closer to unity: 1.13 (Blue), 1.27 (Green) and 1.17 (Red). The A was almost sustained: 5.5% (Blue), 1.2% (Green) and 2.8% (Red). It implies that the bias in AOT affects higher in brighter pixels. If the influence was the same, overall A should be increased to 5.8% (Blue), 1.4% (Green) and 3.0 % (Red) (Figure 17). Thus, the sustained A on 20m bands indicates that the underestimation in brighter pixels were more pronounced than the overestimation in darker pixels. On the overestimated AOT case, similar result was reported (Li et al., 2018). In our data, the AOT seems underestimated so 20m bands looks slightly improved or sustained. When the reverse case happens, however, bias would be increased. On the contrary to the A, the P was reduced a bit: 9.0% (Blue), 7.9% (Green) and 8.1% (Red). Sentinel 2 measures AOT on board and provides AOT map at 60m scale. The improvement in P stems from the reduced uncertainty in AOT. It leads the reduced U and improved R^2. During Sentinel 2 processing, atmospheric correction follows reprojection (Drusch et al., 2012). The bias in atmospheric correction induces the bias on the SR product. The influence varies by the brightness of the pixel. The brighter shows the

more evident bias. Our results show the bias in the atmospheric correction could cause a scale bias even on the SR product.

Sentinel2 (20m)	Satellite SR vs Drone NBAR				Satellite NBAR vs Drone NBAR			
	A (%)	P (%)	U (%)	Q (%)	A (%)	P (%)	U (%)	Q (%)
Blue	7.0	8.9	11.4	67.90	5.5	9.0	10.6	71.96
Green	2.9	7.9	8.4	76.38	1.2	7.9	8.0	80.81
Red	4.4	8.0	9.1	67.53	2.8	8.1	8.5	71.96
RedEdge1	8.3	7.5	11.2	50.55	6.6	7.6	10.1	59.04
RedEdge2	6.1	7.9	10.0	57.93	4.5	8.0	9.2	64.58
RedEdge3	7.4	8.6	11.3	48.71	5.8	8.7	10.4	58.30
Narrow NIR	10.5	8.4	13.5	25.46	8.9	8.5	12.3	36.16
NDVI	12.3	16.4	20.5	25.46	12.2	16.4	20.4	25.46
NIRv	19.6	21.2	28.8	78.60	17.7	21.6	27.9	82.29

Table 7 The same as Table 6 but for Sentinel2 SR and NBAR (20m).
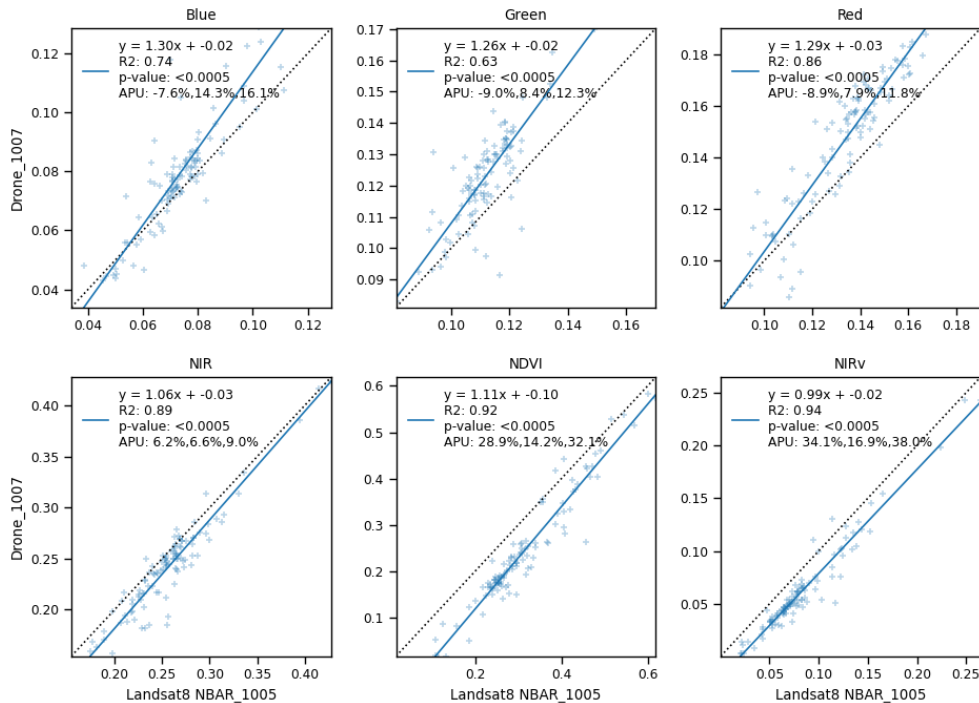
3.2.3 **Landsat 8**

Figure 18 The same as Figure 10 but for Landsat 8 NBAR.
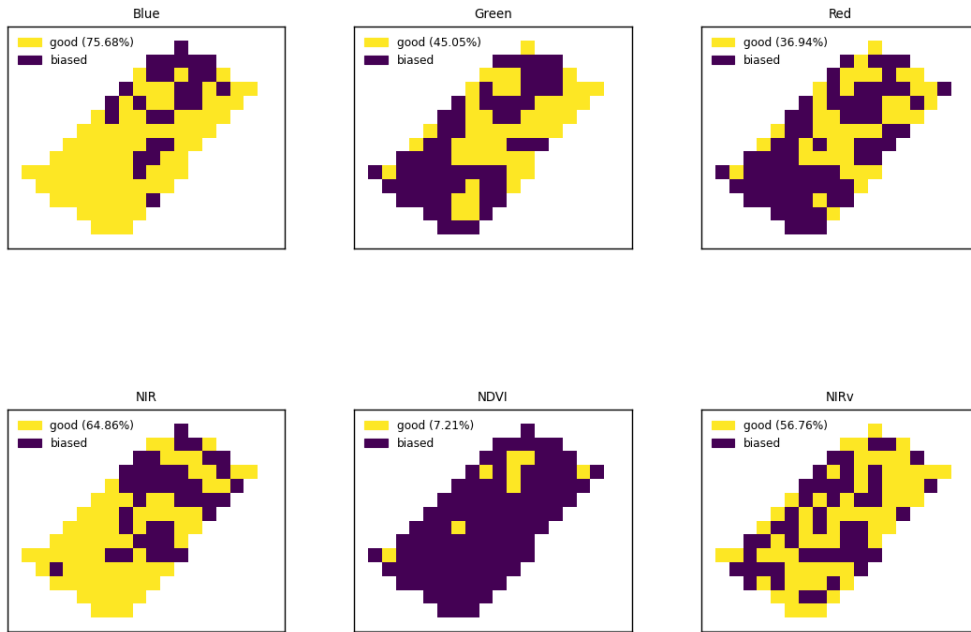
Figure 19 The same as Figure 13 but for Landsat 8 NBAR.

Figure 18 and 19 illustrate the same as Figure 10 and 13, respectively, but for Landsat 8 NBAR. Comparing to Sentinel 2 (20m) NBAR, Landsat 8 NBAR was more biased over the VIS bands with the similar P. Wherein both Sentinel 2 (20m) and Landsat 8 retrieve the AOT for every 3*3 pixel, the P should be comparable with the Sentinel 2 (20m): 14.3% (Blue), 8.4% (Green) and 7.9% (Red). The higher bias could stem from the atmospheric correction algorithm or the atmospheric product: -7.6% (Blue), -9.0% (Green) and -8.9% (Red). Landsat 8 uses LaSRC algorithm for atmospheric correction, which is based on 6S algorithm. LaSRC shows negative bias over VNIR bands (Doxani et al., 2018). It is more biased on Blue and Green, but better performs on Red and NIR (Doxani et al., 2018; Roy et al., 2014). It might affect Blue and Green. However, the Red was also biased where LaSRC is supposed to better perform than Sen2Cor (Doxani et al., 2018). The A is comparable with the Blue and the Green. Thus, the higher bias over VIS bands is due to the failure in retrieving AOT. Lacking of climatology bands, Landsat 8 relies on the auxiliary MODIS dataset (Sayler & Zanter, 2020; Vermote et al., 2016). The AOT inversion and interpolation is based on the accordance of NDVI$_{mid}$ (NDVI which uses shortwave infrared instead of NIR) between Landsat 8 and MODIS (Vermote et al., 2016). Wherein the shortwave infrared bands differ significantly, NDVI$_{mid}$-based interpolation could be problematic (Feng et al., 2012; Claverie et al., 2015). As a result, LaSRC fails to correct AOT at the original scale of 30m. LaSRC was evaluated

at the large scale, 9km * 9km, where the interpolation is not critical (Doxani et al., 2018). Without fine scale AOT products, the better algorithm cannot work well. On the contrary to the VIS, the NIR is more accurate than the Sentinel 2 (20m): 6.2% (NIR). Although the auxiliary data is problematic at fine scale, the NIR band is quite insensitive to water vapor so the original performance was preserved on the NIR (Ke et al., 2015; Lee et al., 2015; Main-Knorn et al., 2017).

Landsat8	Satellite SR vs Drone NBAR				Satellite NBAR vs Drone NBAR			
	A (%)	P (%)	U (%)	Q (%)	A (%)	P (%)	U (%)	Q (%)
Blue	-8.2	14.3	16.4	72.97	-7.6	14.3	16.1	75.68
Green	-9.7	8.4	12.8	39.64	-9	8.4	12.3	45.05
Red	-9.5	7.9	12.4	33.33	-8.9	7.9	11.8	36.94
NIR	5.4	6.6	8.5	65.77	6.3	6.6	9.0	64.86
NDVI	28.8	14.2	32.1	7.21	28.9	14.2	32.1	7.21
NIRv	33.0	16.9	37.1	60.36	34.1	16.9	38.0	56.76

**Table 8** The same as Table 6 but for Landsat 8.

Table 8 summarizes APU matrix and Q of qualified pixels of Landsat 8 SR before and after BRDF normalization. Landsat 8 observed our study area with a VZA of 3° and a RAA of 60° (Table 4). Our study area appeared on the forward scattering region. BRDF normalization adds positive bias on the SR so the NIR rather worsen. Similar to the Sentinel 2, BRDF effect was nominal.

Chapter 4. Conclusion

Although satellite remote sensing features the global coverage, high resolution satellites are also assigned to observe land surface in detail. Referring to HSI, we evaluated Landsat 8 and Sentinel 2 SR product at the original scale. By the traditional validation method, we proved the potential of drone HSI to replace in-situ observations. Over a flat terrain, we compared drone HSI to the satellite SRs and the results to the atmospheric algorithm performances. Our study reveals that 1) the bias in atmospheric parameters leads to the scale bias even on the SR and 2) better atmospheric correction algorithm cannot work properly without fine scale atmospheric products. We demonstrate that the SR product at the original scale could not be generalized from the global analysis. To monitor fine scale dynamics, SR products need to be evaluated at their original scale. This study was limited to the flat terrain which showed less BRDF effect. The influence of the land surface was minor. Over complex terrains with canopy stands (i.e. forest), however, the

surface anisotropy and multiple scattering are expected to affect both drone HSI and satellite SR a lot. More researches are needed to figure out the bias over complex terrains.

Supplemental Materials
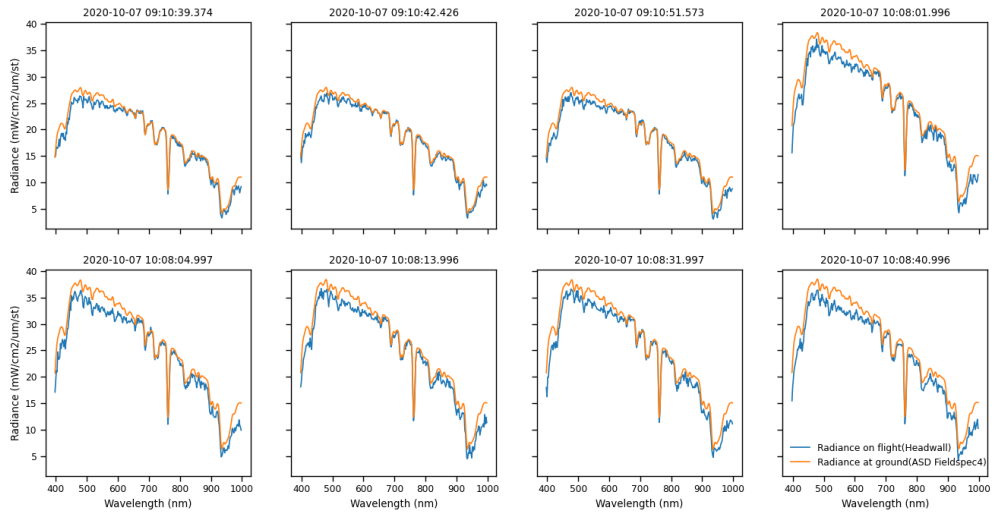
S 1 The comparison between in-situ and on-flight radiance. Orange represents in-situ radiance calculated by ASD Fieldspec4 and Blue represents on-flight radiance measured by Headwall Nano.
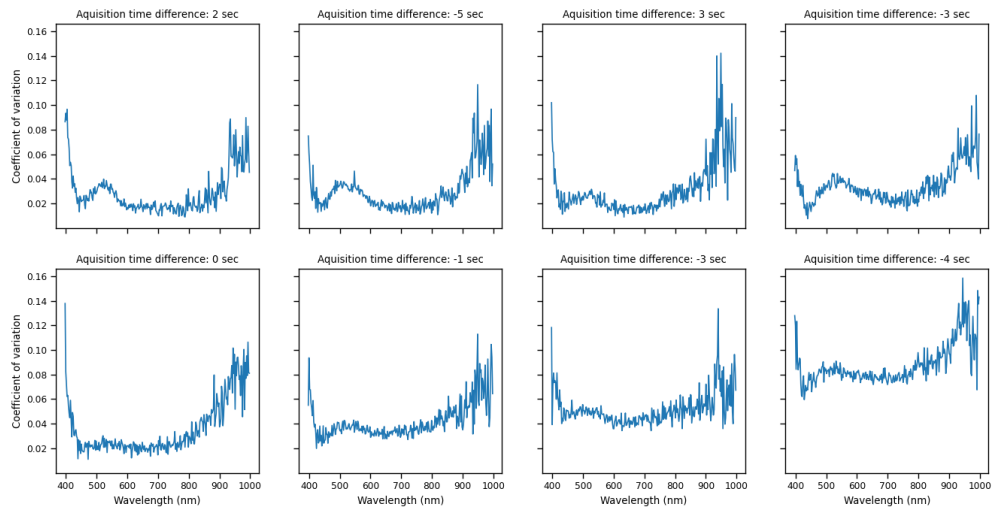
S 2 Each subplot illustrates coefficient of variation on the Spectralon pixels (3*3). The time difference between drone overpassing and ground sampling (Acquisition time difference) falls in 5 seconds.
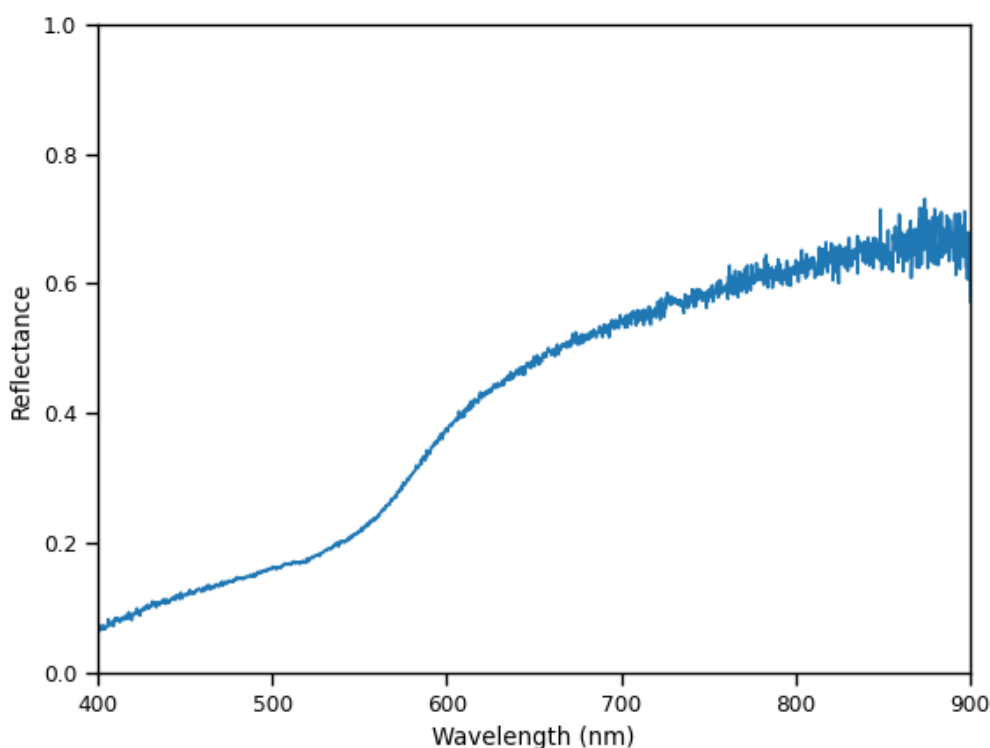
S 3 Reflectance of the sponge cover. On the drone image, the sponge surrounded the Spectralon.
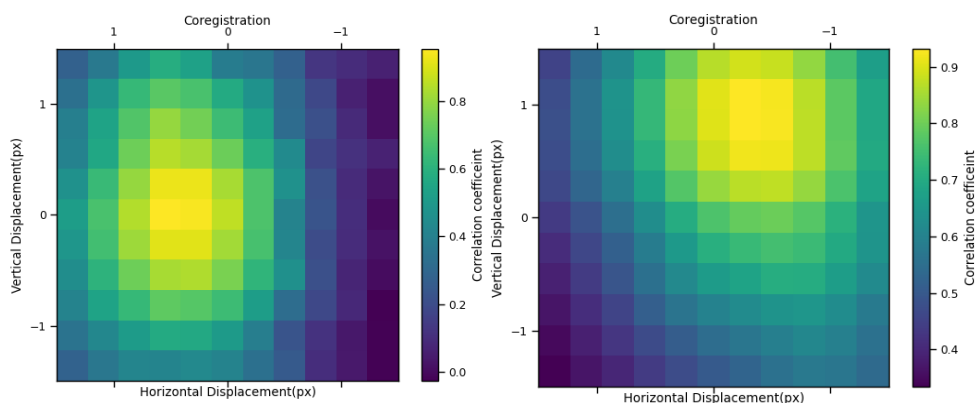
S 4 Automated scene co-registration technique (Houborg & McCabe, 2018). Referring to the satellite NDVI image, drone NDVI map was aligned by increasing the spatial autocorrelation. The color represents correlation coefficient. The left shows the correlation coefficient between drone and Sentinel 2B NDVI by the geographical mismatch and the right shows that between drone and Landsat 8 NDVI.

Drone vs Sentinel2 NBAR		Drone vs Landsat8 NBAR	
Displacement		Displacement	
Horizontal	Vertical	Horizontal	Vertical
-0.3 px (-3 m)	0.9 px (9 m)	0.6 px (18 m)	0 px (0 m)

S 5 The summary of S2. Geographical misregistration between drone and the satellite image
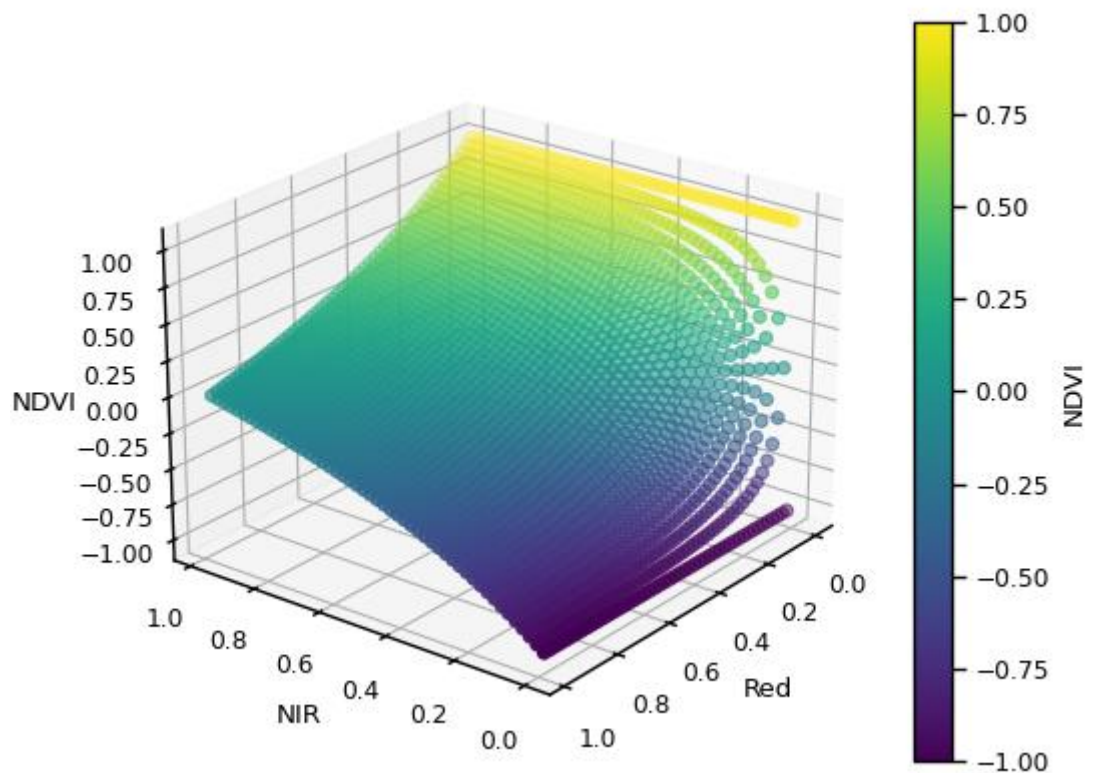
S 6 Sensitivity of NDVI by NIR and Red. Color represents NDVI**.**
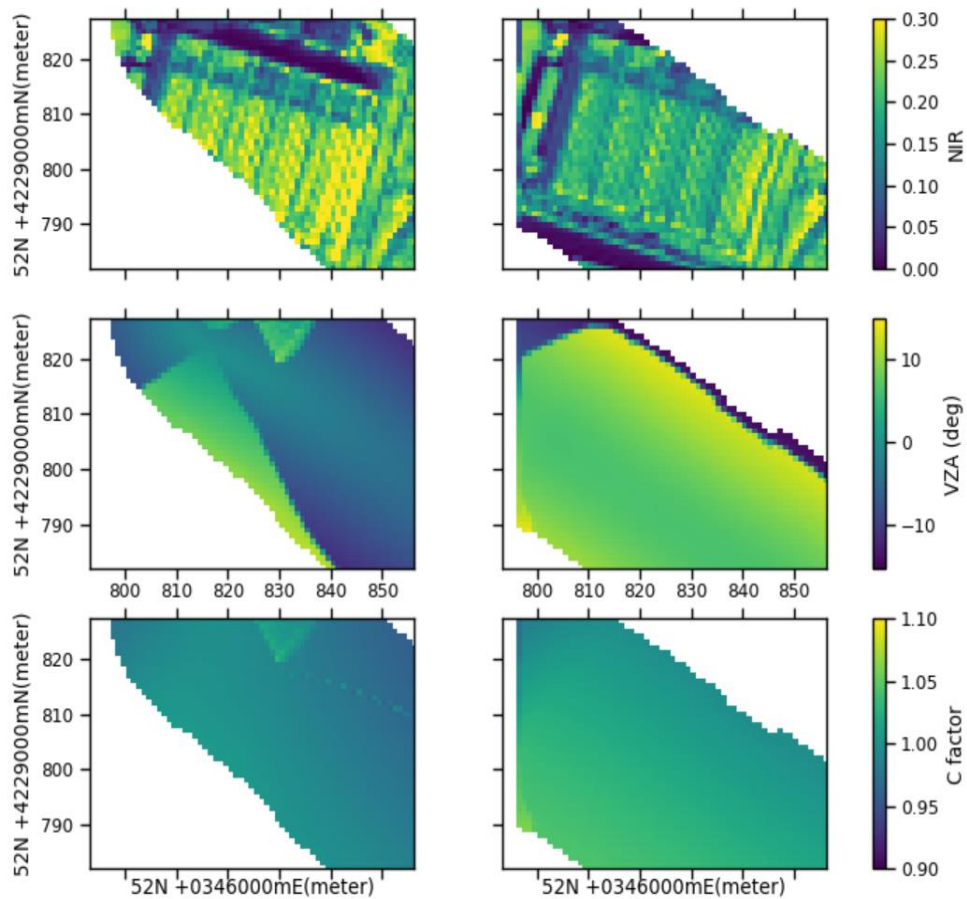
S 7 BRDF effect on glossy rooftop. Two rows represent the two adjacent flight line. The rooftop was observed twice: one on the backward scattering direction (left row) and the other on the forward scattering direction (right row). The first column illustrates NIR reflectance. The second column illustrates view zenith angle: negative values for backward scattering direction. The last column illustrates C factor. C factor is the scaling factor to normalize BRDF effect.

Bibliography

Angel, Y., Turner, D., Parkes, S., Malbeteau, Y., Lucieer, A., & McCabe, M. F. (2020). Automated georectification and mosaicking of UAV-based hyperspectral imagery from push-broom sensors. Remote Sensing, 12(1), 34.

Arroyo-Mora, J. P., Kalacska, M., Løke, T., Schläpfer, D., Coops, N. C., Lucanus, O., & Leblanc, G. (2021). Assessing the impact of illumination on UAV pushbroom hyperspectral imagery collected under various cloud cover conditions. Remote Sensing of Environment, 258, 112396.

Asner, G. P., Martin, R. E., Anderson, C. B., Kryston, K., Vaughn, N., Knapp, D. E., ... & Malhi, Y. (2017). Scale dependence of canopy trait distributions along a tropical forest elevation gradient. New Phytologist, 214(3), 973-988.

Assmann, J. J., Myers-Smith, I. H., Kerby, J. T., Cunliffe, A. M., & Daskalova, G. N. (2020). Drone data reveal heterogeneity in tundra greenness and phenology not captured by satellites. Environmental Research Letters, 15(12), 125002.

Barreto, M. A. P., Johansen, K., Angel, Y., & McCabe, M. F. (2019). Radiometric assessment of a UAV-based push-broom hyperspectral camera. Sensors, 19(21), 4699.

Bay, H., Ess, A., Tuytelaars, T., & Van Gool, L. (2008). Speeded-up robust features (SURF). Computer vision and image understanding, 110(3), 346-359.

Busetto, L., Meroni, M., Crosta, G. F., Guanter, L., & Colombo, R. (2011). SpecCal: Novel software for in-field spectral characterization of high-resolution spectrometers. Computers & geosciences, 37(10), 1685-1691.

Cao, S., Danielson, B., Clare, S., Koenig, S., Campos-Vargas, C., & Sanchez-Azofeifa, A. (2019). Radiometric calibration assessments for UAS-borne multispectral cameras: Laboratory and field protocols. ISPRS Journal of Photogrammetry and Remote Sensing, 149, 132-145.

Claverie, M., Ju, J., Masek, J. G., Dungan, J. L., Vermote, E. F., Roger, J. C., ... & Justice, C. (2018). The Harmonized Landsat and Sentinel-2 surface reflectance data set. Remote sensing of environment, 219, 145-161.

Claverie, M., Vermote, E. F., Franch, B., & Masek, J. G. (2015). Evaluation of the Landsat-5 TM and Landsat-7 ETM+ surface reflectance products. Remote Sensing of Environment, 169, 390-403.

Croft, H., Chen, J. M., Zhang, Y., Simic, A., Noland, T. L., Nesbitt, N., & Arabian, J. (2015). Evaluating leaf chlorophyll content prediction from multispectral remote

sensing data within a physically-based modelling framework. ISPRS Journal of Photogrammetry and Remote Sensing, 102, 85-95.

Curran, P. J. (1989). Remote sensing of foliar chemistry. Remote sensing of environment, 30(3), 271-278.

Di Gennaro, S. F., Dainelli, R., Palliotti, A., Toscano, P., & Matese, A. (2019). Sentinel-2 validation for spatial variability assessment in overhead trellis system viticulture versus UAV and agronomic data. Remote Sensing, 11(21), 2573.

Dixon, D. J., Callow, J. N., Duncan, J. M., Setterfield, S. A., & Pauli, N. (2021). Satellite prediction of forest flowering phenology. Remote Sensing of Environment, 112197.

Doxani, G., Vermote, E., Roger, J. C., Gascon, F., Adriaensen, S., Frantz, D., ... & Vanhellemont, Q. (2018). Atmospheric correction inter-comparison exercise. Remote Sensing, 10(2), 352.

Drusch, M., Del Bello, U., Carlier, S., Colin, O., Fernandez, V., Gascon, F., ... & Bargellini, P. (2012). Sentinel-2: ESA's optical high-resolution mission for GMES operational services. Remote sensing of Environment, 120, 25-36.

Duveiller, G., & Defourny, P. (2010). A conceptual framework to define the spatial resolution requirements for agricultural monitoring using remote sensing. Remote Sensing of Environment, 114(11), 2637-2650.

Fawcett, D., Panigada, C., Tagliabue, G., Boschetti, M., Celesti, M., Evdokimov, A., ... & Anderson, K. (2020). Multi-scale evaluation of drone-based multispectral surface reflectance and vegetation indices in operational conditions. Remote sensing, 12(3), 514.

Feng, M., Huang, C., Channan, S., Vermote, E. F., Masek, J. G., & Townshend, J. R. (2012). Quality assessment of Landsat surface reflectance products using MODIS data. Computers & Geosciences, 38(1), 9-22.

Frantz, D., Haß, E., Uhl, A., Stoffels, J., & Hill, J. (2018). Improvement of the Fmask algorithm for Sentinel-2 images: Separating clouds from bright surfaces based on parallax effects. Remote sensing of environment, 215, 471-481.

Gao, L., Zhan, W., Huang, F., Zhu, X., Zhou, J., Quan, J., ... & Li, M. (2017). Disaggregation of remotely sensed land surface temperature: A simple yet flexible index (SIFI) to assess method performances. Remote Sensing of Environment, 200, 206-219.

Garrigues, S., Allard, D., Baret, F., & Weiss, M. (2006). Quantifying spatial heterogeneity at the landscape scale using variogram models. Remote Sensing of

Environment, 103(1), 81-96.

Garzelli, A., & Nencini, F. (2009). Hypercomplex quality assessment of multi/hyperspectral images. IEEE Geoscience and Remote Sensing Letters, 6(4), 662-665.

Gascon, F., Bouzinac, C., Thépaut, O., Jung, M., Francesconi, B., Louis, J., ... & Fernandez, V. (2017). Copernicus Sentinel-2A calibration and products validation status. Remote Sensing, 9(6), 584.

Griffith, D. A., & Chun, Y. (2016). Spatial autocorrelation and uncertainty associated with remotely-sensed data. Remote Sensing, 8(7), 535.

Habib, A., Han, Y., Xiong, W., He, F., Zhang, Z., & Crawford, M. (2016). Automated ortho-rectification of UAV-based hyperspectral data over an agricultural field using frame RGB imagery. Remote Sensing, 8(10), 796.

Hachtel, J. A., Huang, J., Popovs, I., Jansone-Popova, S., Keum, J. K., Jakowski, J., ... & Idrobo, J. C. (2019). Identification of site-specific isotopic labels by vibrational spectroscopy in the electron microscope. Science, 363(6426), 525-528.

Hakala, T., Markelin, L., Honkavaara, E., Scott, B., Theocharous, T., Nevalainen, O., ... & Fox, N. (2018). Direct reflectance measurements from drones: Sensor absolute radiometric calibration and system tests for forest reflectance characterization. Sensors, 18(5), 1417.

Helder, D., Doelling, D., Bhatt, R., Choi, T., & Barsi, J. (2020). Calibrating Geosynchronous and Polar Orbiting Satellites: Sharing Best Practices. Remote Sensing, 12(17), 2786.

Houborg, R., & McCabe, M. F. (2016a). Adapting a regularized canopy reflectance model (REGFLEC) for the retrieval challenges of dryland agricultural systems. Remote Sensing of Environment, 186, 105-120.

Houborg, R., & McCabe, M. F. (2016b). High-Resolution NDVI from planet's constellation of earth observing nano-satellites: A new data source for precision agriculture. Remote Sensing, 8(9), 768.

Houborg, R., & McCabe, M. F. (2018). A cubesat enabled spatio-temporal enhancement method (cestem) utilizing planet, landsat and modis data. Remote Sensing of Environment, 209, 211-226.

Huete, A. R., Liu, H. Q., Batchily, K. V., & Van Leeuwen, W. J. D. A. (1997). A comparison of vegetation indices over a global set of TM images for EOS-MODIS. Remote sensing of environment, 59(3), 440-451.

Jacquemoud, S., Verhoef, W., Baret, F., Bacour, C., Zarco-Tejada, P. J., Asner, G. P., ... & Ustin, S. L. (2009). PROSPECT+ SAIL models: A review of use for vegetation characterization. Remote sensing of environment, 113, S56-S66.

Jia, W., Pang, Y., Tortini, R., Schläpfer, D., Li, Z., & Roujean, J. L. (2020). A kernel-driven BRDF approach to correct airborne hyperspectral imagery over forested areas with rugged topography. Remote Sensing, 12(3), 432.

Jiang, J., Liu, X., Liu, C., Wu, L., Xia, X., Liu, M., & Du, Z. (2014). Analyzing the spatial scaling bias of rice leaf area index from hyperspectral data using wavelet–fractal technique. IEEE Journal of Selected Topics in Applied Earth Observations and Remote Sensing, 8(6), 3068-3080.

Jiang, R., Wang, P., Xu, Y., Zhou, Z., Luo, X., Lan, Y., ... & Laakso, K. (2020). Assessing the Operation Parameters of a Low-altitude UAV for the Collection of NDVI Values Over a Paddy Rice Field. Remote Sensing, 12(11), 1850.

Kamal, M., Phinn, S., & Johansen, K. (2016). Assessment of multi-resolution image data for mangrove leaf area index mapping. Remote sensing of Environment, 176, 242-254.

Ke, Y., Im, J., Lee, J., Gong, H., & Ryu, Y. (2015). Characteristics of Landsat 8 OLI-derived NDVI by comparison with multiple satellite sensors and in-situ observations. Remote Sensing of Environment, 164, 298-313.

Kimm, H., Guan, K., Jiang, C., Peng, B., Gentry, L. F., Wilkin, S. C., ... & Luo, Y. (2020). Deriving high-spatiotemporal-resolution leaf area index for agroecosystems in the US Corn Belt using Planet Labs CubeSat and STAIR fusion data. Remote Sensing of Environment, 239, 111615.

Kong, J., Ryu, Y., Huang, Y., Dechant, B., Houborg, R., Guan, K., & Zhu, X. (2021). Evaluation of four image fusion NDVI products against in-situ spectral-measurements over a heterogeneous rice paddy landscape. Agricultural and Forest Meteorology, 297, 108255.

Lanconelli, C., Banks, A. C., Muller, J. P., Bruegge, C., Cappucci, F., Gatebe, C., ... & Gobron, N. (2020). In-Situ and Aircraft Reflectance Measurement Effectiveness for CAL/VAL Activities: A Study over Railroad Valley. Remote Sensing, 12(20), 3366.

Lee, C. S., Yeom, J. M., Lee, H. L., Kim, J. J., & Han, K. S. (2015). Sensitivity analysis of 6S-based look-up table for surface reflectance retrieval. Asia-Pacific Journal of Atmospheric Sciences, 51(1), 91-101.

Lehnert, L. W., Meyer, H., Wang, Y., Miehe, G., Thies, B., Reudenbach, C., & Bendix, J. (2015). Retrieval of grassland plant coverage on the Tibetan Plateau based on a

multi-scale, multi-sensor and multi-method approach. Remote sensing of Environment, 164, 197-207.

Li, Y., Chen, J., Ma, Q., Zhang, H. K., & Liu, J. (2018). Evaluation of Sentinel-2A surface reflectance derived using Sen2Cor in North America. IEEE Journal of Selected Topics in Applied Earth Observations and Remote Sensing, 11(6), 1997-2021.

Li, Z., Roy, D. P., Zhang, H. K., Vermote, E. F., & Huang, H. (2019). Evaluation of Landsat-8 and Sentinel-2A aerosol optical depth retrievals across Chinese cities and implications for medium spatial resolution urban aerosol monitoring. Remote sensing, 11(2), 122.

Liu, Y., Wang, T., Ma, L., & Wang, N. (2014). Spectral calibration of hyperspectral data observed from a hyperspectrometer loaded on an unmanned aerial vehicle platform. IEEE Journal of Selected Topics in Applied Earth Observations and Remote Sensing, 7(6), 2630-2638.

Main-Knorn, M., Pflug, B., Louis, J., Debaecker, V., Müller-Wilm, U., & Gascon, F. (2017). Sen2Cor for sentinel-2. In Image and Signal Processing for Remote Sensing XXIII (Vol. 10427, p. 1042704). International Society for Optics and Photonics.

Meroni, M., Busetto, L., Guanter, L., Cogliati, S., Crosta, G. F., Migliavacca, M., ... & Colombo, R. (2010). Characterization of fine resolution field spectrometers using solar Fraunhofer lines and atmospheric absorption features. Applied optics, 49(15), 2858-2871.

Messina, G., Peña, J. M., Vizzari, M., & Modica, G. (2020). A Comparison of UAV and Satellites Multispectral Imagery in Monitoring Onion Crop. An Application in the 'Cipolla Rossa di Tropea'(Italy). Remote Sensing, 12(20), 3424.

Myers-Smith, I. H., Kerby, J. T., Phoenix, G. K., Bjerke, J. W., Epstein, H. E., Assmann, J. J., ... & Berner, L. T. (2020). Complexity revealed in the greening of the Arctic. Nature Climate Change, 10(2), 106-117.

Padró, J. C., Muñoz, F. J., Ávila, L. Á., Pesquer, L., & Pons, X. (2018). Radiometric correction of Landsat-8 and Sentinel-2A scenes using drone imagery in synergy with field spectroradiometry. Remote Sensing, 10(11), 1687.

Peng, J., Liu, Q., Wang, L., Liu, Q., Fan, W., Lu, M., & Wen, J. (2015). Characterizing the pixel footprint of satellite albedo products derived from MODIS reflectance in the Heihe River Basin, China. Remote Sensing, 7(6), 6886-6907.

Pflug, B., & Main-Knorn, M. (2014, October). Validation of atmospheric correction algorithm ATCOR. In Remote sensing of clouds and the atmosphere XIX; and optics in atmospheric propagation and adaptive systems XVII (Vol. 9242, p. 92420W).

International Society for Optics and Photonics.

Pillay, R., Hardeberg, J. Y., & George, S. (2019). Hyperspectral imaging of art: Acquisition and calibration workflows. Journal of the American Institute for Conservation, 58(1-2), 3-15.

Planet, 2021. PLANET IMAGERY PRODUCT SPECIFICATIONS [WWW Document]. https://assets.c.com/docs/Planet_Combined_Imagery_Product_Specs_letter_screen.pdf (accessed 21.02.25)

Radoux, J., Chomé, G., Jacques, D. C., Waldner, F., Bellemans, N., Matton, N., ... & Defourny, P. (2016). Sentinel-2's potential for sub-pixel landscape feature detection. Remote Sensing, 8(6), 488.

Rocha, A. D., Groen, T. A., & Skidmore, A. K. (2019). Spatially-explicit modelling with support of hyperspectral data can improve prediction of plant traits. Remote sensing of environment, 231, 111200.

Rocha, A. D., Groen, T. A., Skidmore, A. K., Darvishzadeh, R., & Willemen, L. (2018). Machine learning using hyperspectral data inaccurately predicts plant traits under spatial dependency. Remote sensing, 10(8), 1263.

Román, M. O., Gatebe, C. K., Schaaf, C. B., Poudyal, R., Wang, Z., & King, M. D. (2011). Variability in surface BRDF at different spatial scales (30 m–500 m) over a mixed agricultural landscape as retrieved from airborne and satellite spectral measurements. Remote Sensing of Environment, 115(9), 2184-2203.

Roujean, J. L., Leroy, M., & Deschamps, P. Y. (1992). A bidirectional reflectance model of the Earth's surface for the correction of remote sensing data. Journal of Geophysical Research: Atmospheres, 97(D18), 20455-20468.

Roy, D. P., Kovalskyy, V., Zhang, H. K., Vermote, E. F., Yan, L., Kumar, S. S., & Egorov, A. (2016a). Characterization of Landsat-7 to Landsat-8 reflective wavelength and normalized difference vegetation index continuity. Remote sensing of Environment, 185, 57-70.

Roy, D. P., Li, J., Zhang, H. K., & Yan, L. (2016b). Best practices for the reprojection and resampling of Sentinel-2 Multi Spectral Instrument Level 1C data. Remote Sensing Letters, 7(11), 1023-1032.

Roy, D. P., Li, J., Zhang, H. K., Yan, L., Huang, H., & Li, Z. (2017b). Examination of Sentinel-2A multi-spectral instrument (MSI) reflectance anisotropy and the suitability of a general method to normalize MSI reflectance to nadir BRDF adjusted reflectance. Remote Sensing of Environment, 199, 25-38.

Roy, D. P., Li, Z., & Zhang, H. K. (2017a). Adjustment of Sentinel-2 multi-spectral instrument (MSI) Red-Edge band reflectance to Nadir BRDF adjusted reflectance (NBAR) and quantification of red-edge band BRDF effects. Remote Sensing, 9(12), 1325.

Roy, D. P., Wulder, M. A., Loveland, T. R., Woodcock, C. E., Allen, R. G., Anderson, M. C., ... & Zhu, Z. (2014). Landsat-8: Science and product vision for terrestrial global change research. Remote sensing of Environment, 145, 154-172.

Roy, D. P., Zhang, H. K., Ju, J., Gomez-Dans, J. L., Lewis, P. E., Schaaf, C. B., ... & Kovalskyy, V. (2016c). A general method to normalize Landsat reflectance data to nadir BRDF adjusted reflectance. Remote Sensing of Environment, 176, 255-271.

Ryu, Y., Kang, S., Moon, S. K., & Kim, J. (2008). Evaluation of land surface radiation balance derived from moderate resolution imaging spectroradiometer (MODIS) over complex terrain and heterogeneous landscape on clear sky days. agricultural and forest meteorology, 148(10), 1538-1552.

Sayler, K. & Zanter, K. (2020). Surface Reflectance Code (LASRC) Product Guide. USGS and NASA: Reston, VA, USA.

Schaepman-Strub, G., Schaepman, M. E., Painter, T. H., Dangel, S., & Martonchik, J. V. (2006). Reflectance quantities in optical remote sensing—Definitions and case studies. Remote sensing of environment, 103(1), 27-42.

Seidel, F. C., Stavros, E. N., Cable, M. L., Green, R., & Freeman, A. (2018). Imaging spectrometer emulates landsat: a case study with airborne visible infrared imaging spectrometer (AVIRIS) and operational land imager (OLI) data. Remote Sensing of Environment, 215, 157-169.

Siewert, M. B., & Olofsson, J. (2020). Scale-dependency of Arctic ecosystem properties revealed by UAV. Environmental Research Letters, 15(9), 094030.

Sola, I., García-Martín, A., Sandonís-Pozo, L., Álvarez-Mozos, J., Pérez-Cabello, F., González-Audícana, M., & Llovería, R. M. (2018). Assessment of atmospheric correction methods for Sentinel-2 images in Mediterranean landscapes. International journal of applied earth observation and geoinformation, 73, 63-76.

Strahler, A. H., Muller, J., Lucht, W., Schaaf, C., Tsang, T., Gao, F., ... & Barnsley, M. J. (1999). MODIS BRDF/albedo product: algorithm theoretical basis document version 5.0. MODIS documentation, 23(4), 42-47.

Tan, B., Woodcock, C. E., Hu, J., Zhang, P., Ozdogan, M., Huang, D., ... & Myneni, R. B. (2006). The impact of gridding artifacts on the local spatial properties of MODIS data: Implications for validation, compositing, and band-to-band registration across

resolutions. Remote Sensing of Environment, 105(2), 98-114.

Tan, K., Niu, C., Jia, X., Ou, D., Chen, Y., & Lei, S. (2020). Complete and accurate data correction for seamless mosaicking of airborne hyperspectral images: A case study at a mining site in Inner Mongolia, China. ISPRS Journal of Photogrammetry and Remote Sensing, 165, 1-15.

Teillet, P. M. (1997). A status overview of earth observation calibration/validation for terrestrial applications. Canadian Journal of Remote Sensing, 23(4), 291-298.

Teillet, P. M., Fedosejevs, G., Thome, K. J., & Barker, J. L. (2007). Impacts of spectral band difference effects on radiometric cross-calibration between satellite sensors in the solar-reflective spectral domain. Remote Sensing of Environment, 110(3), 393-409.

Teixeira Pinto, C., Jing, X., & Leigh, L. (2020). Evaluation Analysis of Landsat Level-1 and Level-2 Data Products Using In Situ Measurements. Remote Sensing, 12(16), 2597.

Trishchenko, A. P., Cihlar, J., & Li, Z. (2002). Effects of spectral response function on surface reflectance and NDVI measured with moderate resolution satellite sensors. Remote Sensing of Environment, 81(1), 1-18.

Vermote, E. F., & Kotchenova, S. (2008). Atmospheric correction for the monitoring of land surfaces. Journal of Geophysical Research: Atmospheres, 113(D23).

Vermote, E., Roger, J. C., Franch, B., & Skakun, S. (2018). LaSRC (Land Surface Reflectance Code): Overview, application and validation using MODIS, VIIRS, LANDSAT and Sentinel 2 data's. In IGARSS 2018-2018 IEEE International Geoscience and Remote Sensing Symposium (pp. 8173-8176). IEEE.

Vrieling, A., Meroni, M., Darvishzadeh, R., Skidmore, A. K., Wang, T., Zurita-Milla, R., ... & Paganini, M. (2018). Vegetation phenology from Sentinel-2 and field cameras for a Dutch barrier island. Remote sensing of environment, 215, 517-529.

Wang, Q., & Atkinson, P. M. (2017). The effect of the point spread function on sub-pixel mapping. Remote Sensing of Environment, 193, 127-137.

Wang, Z., Schaaf, C. B., Strahler, A. H., Chopping, M. J., Román, M. O., Shuai, Y., ... & Fitzjarrald, D. R. (2014). Evaluation of MODIS albedo product (MCD43A) over grassland, agriculture and forest surface types during dormant and snow-covered periods. Remote Sensing of Environment, 140, 60-77.

Wenny, B. N., Helder, D., Hong, J., Leigh, L., Thome, K. J., & Reuter, D. (2015). Pre- and post-launch spatial quality of the Landsat 8 Thermal Infrared Sensor. Remote

Sensing, 7(2), 1962-1980.

Williams, L. J., Cavender-Bares, J., Townsend, P. A., Couture, J. J., Wang, Z., Stefanski, A., ... & Reich, P. B. (2021). Remote spectral detection of biodiversity effects on forest biomass. Nature Ecology & Evolution, 5(1), 46-54.

Wu, S., Wang, J., Yan, Z., Song, G., Chen, Y., Ma, Q., ... & Wu, J. (2021). Monitoring tree-crown scale autumn leaf phenology in a temperate forest with an integration of PlanetScope and drone remote sensing observations. ISPRS Journal of Photogrammetry and Remote Sensing, 171, 36-48.

Yan, L., Roy, D. P., Zhang, H., Li, J., & Huang, H. (2016). An automated approach for sub-pixel registration of Landsat-8 Operational Land Imager (OLI) and Sentinel-2 Multi Spectral Instrument (MSI) imagery. Remote Sensing, 8(6), 520.

Yang, K., Ryu, Y., Dechant, B., Berry, J. A., Hwang, Y., Jiang, C., ... & Yang, X. (2018). Sun-induced chlorophyll fluorescence is more strongly related to absorbed light than to photosynthesis at half-hourly resolution in a rice paddy. Remote Sensing of Environment, 216, 658-673.

Zanter K. (2019). Landsat 8 (L8) data users handbook. LSDS-1574 Version 5.0 [WWW Document]. https://www.usgs.gov/media/files/landsat-8-data-users-handbook (accessed 21.02.25)

Zhang, X., Wang, J., Gao, F., Liu, Y., Schaaf, C., Friedl, M., ... & Yan, D. (2017). Exploration of scaling effects on coarse resolution land surface phenology. Remote Sensing of Environment, 190, 318-330.

Abstract in Korean

원격탐사에서 지표 반사도(SR)는 지표정보를 비파괴적이고 즉각적인 방법으로 전달해주는 매개체 역할을 한다. 신뢰할 수 있는 SR은 육상 생태계 모델링의 기본이고, 이에 따라 SR의 시공간적 검증이 요구된다. 일반적으로 SR은 여러 지상 기준점(GCP)을 기반으로 하는 현장 분광법을 통해서 시간적 연속성이 보장된다. 그러나 현장 분광법은 제한적인 샘플링으로 공간 패턴을 거의 보여주지 않아, 위성 SR의 픽셀 별 공간 변동성은 잘 분석되지 않았다. 본 연구에서는 드론 기반의 초분광 영상(HSI)을 참고자료로 도입하여, 이를 이질적인 논 경관에서 Sentinel 2 및 Landsat 8 SR과 비교하였다. 우선, 드론 HSI는 현장 분광법 및 경로 중첩을 통해서 관측각도 범위 내에서 정성적인 방사 측정을 보장한다고 검증되었다. 이후, 드론 HSI는 위성 SR의 분광반응특성, 공간해상도 및 좌표계를 기준으로 맞춰졌고, 관측 기하를 통일하기 위해서 드론 HIS와 위성 SR은 각각 양방향반사율분포함수 (BRDF) 정규화 반사도 (NBAR)로 변환되었다. 마지막으로, 1) APU 행렬로 위성 SR과 NDVI, NIRv를 포함하는 식생지수(VI)의 공간변동성을 정량화 했고, 2) 대기보정의 이론적 오차를 기준으로 SR과 VI를 픽셀별로 평가했고, 3) BRDF 정규화를 통한 개선 사항을 검토했다.

Sentinel 2 SR은 드론 HSI와 전반적으로 좋은 일치를 보이나, 두 NIR 채널은 최대 10% 편향되었다. NIR의 편향은 식생지수에서 토지 피복에 따라 다른 영향을 미쳤다. NDVI는 식생에서는 낮은 편향을 보여줬고, NIRv는 도시시설물 영역에서만 높은 편향을 보였다. Landsat 8 SR은 VIS 채널에 대해 편향되었다 (-9 ~ -7.6%). BRDF 정규화는 위성 SR의 품질을 개선했지만, 그 영향은 부수적이었다. 본 연구에서는 평탄한 지형에서 드론 HSI가 현장 관측을 대체할 수 있고, 따라서 위성 SR이나 대기보정 알고리즘을 평가하는데 활용될 수 있다는 것을 보였다. 향후 연구에서는 산림으로 대상지를 확대하여, 지형과 캐노피 구조가 드론 HSI 및 위성 SR에 미치는 영향을 분석할 필요가 있다.